university of groningen / faculty of mathematics and natural sciences / zernike institute for advanced materials

BACHELOR'S THESIS

Spin polarized transport in a magnetic tunnel junction with an oxide barrier

Author:
Miranda Jacqueline BUIL CONTRERAS

Supervisor:
Prof. Dr. T. BANERJEE
Daily Supervisor:
A. JAMAN
Referent:
Prof. Dr. C. H. VAN DER WAL

UNIVERSITY OF GRONINGEN

in the

Spintronics of Functional Materials
Zernike Institute for Advanced Materials

July 2023

UNIVERSITY OF GRONINGEN

Abstract

Physics

Zernike Institute for Advanced Materials

Bachelor

Spin polarized transport in a magnetic tunnel junction with an oxide barrier

by Miranda Jacqueline BUIL CONTRERAS

This research focuses on the fabrication of MTJ (Magnetic Tunnel Junction) devices using different materials, with the aim of measuring their tunneling magnetoresistance ratio. One of the materials used is $La_{2/3}Sr_{1/3}MnO_3$, a ferromagnetic cubic perovskite manganate known for its 100% spin polarization, which can greatly enhance the efficiency of spintronic devices by contributing to highly spin polarized current.

Three FM/I/FM stacks are fabricated, with $La_{2/3}Sr_{1/3}MnO_3$ serving as the bottom layer and $SrTiO_3$ as the insulating layer. The structural, magnetic, and electrical properties of these stacks are extensively investigated using techniques such as atomic force microscopy, reflective high-energy electron diffraction, x-ray diffraction, and magnetic properties measurement systems.

Among the fabricated samples, the LSMO/STO/Co stack exhibits the highest quality of growth, although all samples meet the necessary quality standards. Suggestions about how to further complete the study to obtain a more comprehensive understanding of the investigated systems are presented.

Contents

List of Figures

Chapter 1

Introduction

Nowadays, there is an increasing trend towards down-scaling chips in order to make smaller, faster, and more efficient computers. A difficulty risen by down-scaling is the power leakage found in currently used technology [3]. This is caused by the flow of current even when the device is inactive. Spin-based devices are good way to approach this matter because they are able to use spin polarized current. Spintronics makes use of the information carried by the spin of the electron instead of its charge. This allows combining traditional electronic features with spin-dependent effects which come from the interaction between the spin of the carrier and the magnetic medium that it travels [4], for instance, spin-polarized current.

Given their potential applications in this field, magnetic tunnel junctions (MTJ) have gained attention over recent years. They can be used in magnetic random access memories, tunneling magnetoresistance (TMR) read heads, and magnetic field sensors among others [5]. A MTJ is a heterostructure composed of an insulating barrier sandwiched by two ferromagnetic electrodes. By applying a bias between the electrodes tunneling of electrons occurs across the barrier. The resistance caused by spin-polarized tunneling can be modulated by changing the magnetization direction of the electrodes relative to each other, this effect is called tunneling magnetoresistance. A high TMR ratio is obtained if the ferromagnetic electrodes have high values of spin polarization [6]. $La_{2/3}Sr_{1/3}MnO_3$ (LSMO) is a promising bottom electrode for a MTJ since it is a half-metal, theoretically providing 100% spin polarisation. In addition, LSMO presents significantly large changes in resistance when a magnetic field is applied, the so-called colossal magnetoresistance (CMR) [5].

In this study, three FM/I/FM stacks were grown using LSMO as a bottom ferromagnetic layer and $SrTiO_3$ as a tunnel barrier. Different materials were used to complete the trilayers, among which there is Co and LSMO. The aim of this project is to fabricate MTJ devices, with the mentioned materials, in order to study their structural characterization and measure their magnetic and electrical properties. A comparison between all devices will then be performed.

An introduction to the theoretical concepts surrounding MTJs will be done in chapter 1. Thereafter, the fabrication and characterization methods will be explained in chapter 3.

The results obtained from the aforementioned methods will be discussed in chapter 4. Finally, chapter 5 will contain the conclusion arrived at.

Chapter 2

Theory

2.1 $La_{1-x}Sr_xMnO_3$

$La_{1-x}Sr_xMnO_3$ follows the ABO_3 manganese perovskite structure with lattice parameter a = 3.87 Å represented in figure 2.1, where A corresponds to the rare earth ions La and Sr, B is the Mn ion and O are the oxygen anions. The divalent Mn cation is found in the center of a face-centered cubic structure, where the La/Sr cations are in the corners, and the oxygen anions are at the faces forming an octahedra around Mn [7]. The valence of the Mn ion is determined by the La/Sr doping elements in order to make the system neutrally charged.

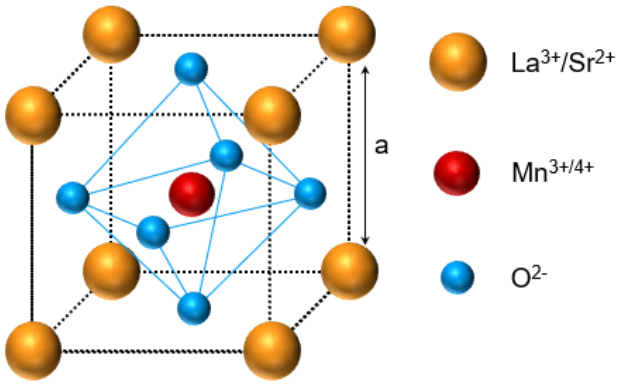

FIGURE 2.1: Crystal structure of the LSMO perovskite structure. The Mn^{3+} or Mn^{4+} are situated in the center surrounded by an O^{2-} octahedra while La^{3+} and Sr^{2+} are found in the corners.

The Goldschmidt tolerance factor $t = (r_A + r_O)/\sqrt{2}(r_B + r_O)$ governs the structure of the manganites, where r_A, r_B, and r_O are the respective ionic radii. In order for the perovskite to be stable, t should not deviate too much from 1, corresponding to a perfect closely packed cubic structure [8]. This can be useful when studying the compatibility between crystals and ions.

2.1.1 Half-metallicity

In spintronic applications like MTJs, the highest magnetoresistance effects are observed for the currents with the highest level of spin polarization. As a result, numerous ongoing research works are dedicated to discovering a ferromagnetic material that exhibits complete spin polarization. Half-metallic ferromagnetic materials emerge as promising contenders in this pursuit [9].

Half-metallic materials have a peculiar electronic structure. Looking at the spin density of states (DOS), for one spin direction the structure will be of a metal, where the Fermi energy lies on the conduction band, while for the other spin channel, the Fermi energy will lie at a gap, like in semiconductors or insulators [10]. This is illustrated in figure 2.2. LSMO is an optimally-doped manganite that presents half-metallicity. An important factor about it is that the spin-up states are the allowed ones at the Fermi level.

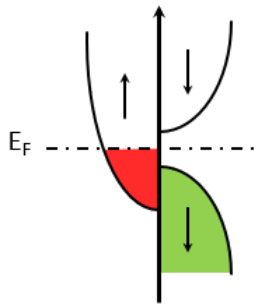

FIGURE 2.2: DOS schematic of a half metal where E_F is the Fermi energy.

A criterion that half-metals in stoichiometric compounds have to follow is the integer spin moment criterion. Since a half-metal only has allowed states for one spin channel at the Fermi energy, the number of allowed states of that channel will be an integer. The sum of spin-up and spin-down allowed states is an integer as well, so it follows that the number of spin-up and spin-down states separately are integers too. This implies that the difference in the number of spin states at the Fermi level needs to be an integer value. Verifying this provides a straightforward means of identifying half-metals. Nevertheless, beyond this step, it becomes challenging to pinpoint precise methods for determining half-metallicity due to limitations in experimentation. A factor that can develop in the destruction of half-metallicity is crystallographic disorder [11], so high-quality films are needed if this effect is to be observed.

Generally, half-metals have a low Curie temperature which makes them impractical for usage in devices. Another impediment is that spin polarization decreases with increasing temperature [11].

2.2 Exchange interactions

2.2.1 Double-exchange

In LSMO, double-exchange mechanism occurs between adjacent Mn ions of different valence mediated by an O ion, illustrated in figure 2.3. It consists of a simultaneous transfer of two electrons of the same spin, one from Mn^{3+} to O^{2-}, and the other to Mn^{4+}. This mechanism leads to ferromagnetism, as electron transfer is only possible if the moments of the Mn cations are aligned in order to satisfy Hund's rule. The hopping contributes to the conductivity of the crystal [12].

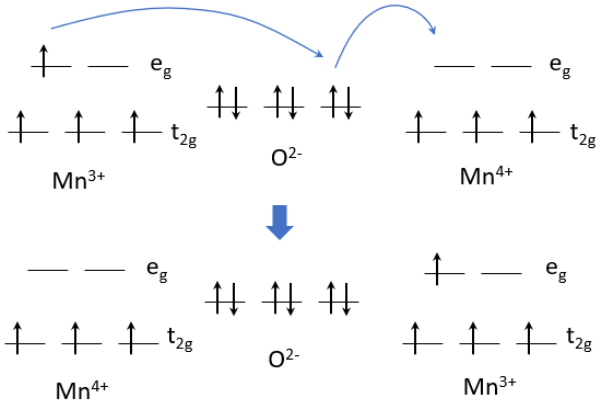

FIGURE 2.3: Double exchange mechanism

2.2.2 Super-exchange

In a Mn^{3+}-O^{2-}-Mn^{3+} it can be assumed that the bonding is mainly ionic, where the Mn cations have 4 electrons in the 3d shell and the O anions have 6 electrons in the 2p shell. Assuming it is energetically favorable to have some covalent intermixing, 2 electrons from the O 2p shell would be shared with the Mn ions (one each), and this shall follow Pauli's exclusion principle. In this case, the Mn^{3+} 3d shell is less than half filled, so the electrons transferred from O 2p shell will align parallel with the 3d electrons, as illustrated in figure 2.4. In order to satisfy Pauli's principle, the spins of the Mn cations must be antiparallel, giving rise to antiferromagnetic coupling. This interaction is strongest if the angle between both cations is 180º [12].

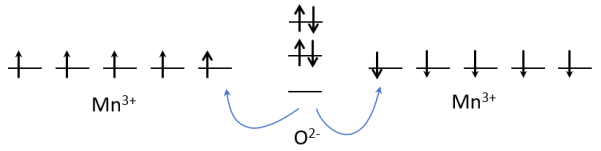

FIGURE 2.4: Super-exchange mechanism

2.3 Phase diagram

Many factors contribute to the magnetic and electric properties of LSMO among which the exchange interactions are found. The phase diagram of $La_{1-x}Sr_xMnO_3$ is shown in figure 2.5, where the x axis represents the amount of doping and the y axis is the temperature. Starting at x = 0, the resultant complex oxide would be $LaMnO_3$, which is a paramagnetic insulator at room temperature (300 K). As the material is doped, LSMO is obtained, which has its highest T_C at x $\approx$ 0.33 in the ferromagnetic metal regime. If the doping continues to be increased, the paramagnetic metal regime will be achieved. In this project, the doping level of x = 1/3 or 0.33 will be used as it provides a high T_C and a ferromagnetic metal phase, which is needed for the purpose.

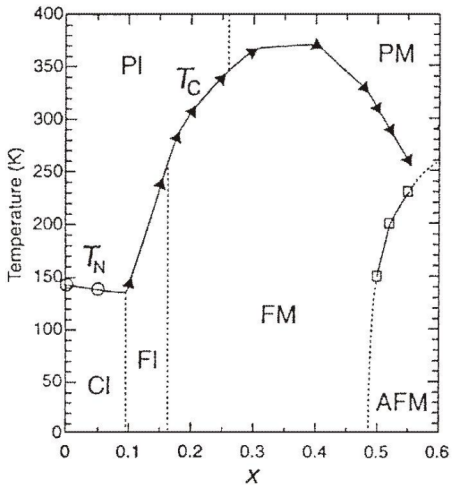

FIGURE 2.5: Phase diagram of $La_{1-x}Sr_xMnO_3$ (made by [1]) where the known phases are plotted in terms of the amount of doping (x) and the Curie temperature. The black line with the arrows denotes the curie temperature (T_C) and the dotted lines the separation between phases. AFM, FM, FI, CI, PI and PM mean antiferromagnetic metal, ferromagnetic metal, ferromagnetic insulator, spin-canted insulator, paramagnetic insulator, and paramagnetic metal respectively [2].

2.4 Magnetic Tunnel Junctions

The magnetization of the ferromagnets can be manipulated by an external magnetic field. The ferromagnets are chosen to have different coercivities so that they will change magnetization at different values of an external magnetic field. Consequently, there will exist a parallel state (magnetizations pointing in the same direction), and an antiparallel state (magnetizations in opposite directions). By applying a bias, electrons can tunnel through the barrier. Spin-polarized tunneling will occur due to the relative magnetization of the ferromagnets. This relationship is called tunneling magnetoresistance. MTJ are important because they have shown relative magnetoresistance of several hundred percent [13]. There is another finding, that allows switching the state of an MTJ using spin-polarized current instead of an external magnetic field, called spin-transfer torque effect (STT). Due

to its use of the same line for reading and writing, it allows for a simpler, denser, and more scalable design. The magnetizations of the ferromagnets can also be perpendicular or parallel to the film, bringing different advantages. The former allows for switching using a localized magnetic field, while the latter might solve this issue by reducing the size.

Given the high relative magnetoresistance, nonvolatility, high write speed, and good scalability, MTJ has found applications like its incorporation to hard-disk-drive read heads, which has expanded the hard-disk recording. In addition, MTJs can be used in magnetic random access memories, where it would include the high density of dynamic random-access memories, the nonvolatility of the flash memory, and the speed in read and write of static random-access memory [13].

2.5 Tunneling Magnetoresistance

Spin-dependent tunneling (SDT) results in TMR. SDT arises from an imbalance of spin in the tunneling current between the top and bottom ferromagnets through the tunnel barrier. This relationship was explained by Julliere's model where he made two main assumptions. Firstly, it was assumed that spin is conserved in tunneling. It is then implied that the tunneling process happens through two independent spin channels (up and down) close to the Fermi energy. The filled up (down) states of one electrode would be allowed to tunnel to the empty up (down) of the other electrode. In a configuration where the ferromagnets have parallel magnetizations, spins would be tunneling from majority states to majority states. If the magnetizations are antiparallel, they would travel from a majority state to a minority state of each ferromagnet and vice versa. Secondly, he assumed that the tunneling probability was proportional to the product of the spin density of states for each spin channel [6]. So in a configuration where the majority states in both ferromagnets have the same spin, tunneling would be more likely, and if the same spin is the majority state in one ferromagnet, and minority state in the other, tunneling would occur less, this is shown in figure 2.6. One way to describe the TMR ratio is given by

$$TMR = \frac{2P_1P_2}{1 - P_1P_2} \tag{2.1}$$

where P_1 and P_2 are the spin polarization of the top and bottom ferromagnets. Spin polarisation is defined as

$$P = \frac{n^{\uparrow} - n^{\downarrow}}{n^{\uparrow} + n^{\downarrow}} \tag{2.2}$$

where $n^{\uparrow}$ is the density of states of the spin-up states and $n^{\downarrow}$ of the spin-down states [6]. An important assumption used for this project is that tunneling is independent of the barrier choice.

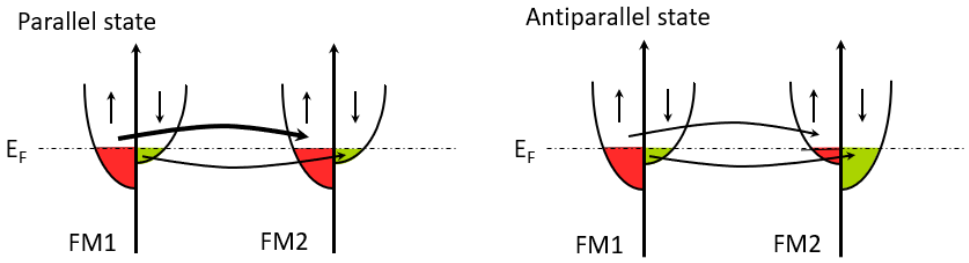

FIGURE 2.6: Density of states plots for the parallel (left) and antiparallel (right) configurations of the ferromagnet's magnetizations. The thickness of the arrows from one ferromagnet to the other signifies tunneling probability, eg. in the parallel state tunneling is very likely between both up states and not so much between the down states.

2.5.1 Positive and negative TMR

Depending on the interface materials in an MTJ the TMR observed can be positive or negative. Positive or negative TMR refers to the change in resistance when a magnetic field is applied, where positive corresponds to the system where the parallel configuration is that of low resistance and the antiparallel of high resistance, and the opposite for negative TMR. Studies where MTJ were epitaxially grown [14] have shown that, even though Co has a positive effective spin polarization (majority spin up) in contact with aluminum oxide, it has a negative one if STO is used. *Ab initio* calculations suggest that this is due to an sp-d bonding mechanism between Co and Al. Similarly, for the STO-Co interface, the negative polarization is attributed to d-d bonding effects between Al and Ti. On the other hand, it has been seen that if the layers of the MTJ are amorphous (for the same Co-STO interface), a positive TMR ratio is observed [15]. From this, it is evident that the electronic and crystal structure at metal-oxide interfaces has a relevant role in the spin polarization of the tunneling charge.

2.6 Simmons equation

Sommerfield and Bethe were the first ones to study the tunneling behavior in MTJs for very high voltages assuming a square barrier. Further studies were performed that improved their description by approximating the barrier to a parabola or by using an intermediate voltage range. The Simmons model aims to describe tunneling through a metal/insulator/metal system for a generalized barrier, which allows using high, intermediate,and low voltage range [16]. The intermediate voltage equation is given by

$$J(V,T) = J(V,0)\left\{1 + \frac{3\times 10^{-9} s^2 T^2}{\phi_0 - \frac{V}{2}}\right\} \tag{2.3}$$

where $J(V,0)$ is described by

$$\begin{aligned} J(V) = &\left[\frac{6.2\times10^{10}}{s^2}\right]\left(\phi_0 - \frac{V}{2}\right)\exp\left[-1.025s\left(\phi_0 - \frac{V}{2}\right)^{\frac{1}{2}}\right] \\ &- \left[\frac{6.2\times10^{10}}{s^2}\right]\left(\phi_0 + \frac{V}{2}\right)\exp\left[-1.025s\left(\phi_0 + \frac{V}{2}\right)^{\frac{1}{2}}\right] \end{aligned} \tag{2.4}$$

where $J(V,T)$ is the tunnel current density in terms of voltage and temperature, $J(V,0)$ only in terms of voltage, s is the thickness of the insulating barrier, T is the temperature, ϕ_0 is the height of the potential barrier, and V is the voltage.

Chapter 3

Experimental methods

3.1 Substrate preparation

In thin film growth, defects and other imperfections in the substrate can strongly impact the quality and the properties that the stack will have. That is why it is important to adequately prepare the substrate in order to optimize growth.

3.1.1 TiO_2 termination

$SrTiO_3$ is a perovskite oxide composed of alternating layers of TiO_2 and SrO in the 100 direction. SrO is reactive with H_2O and CO_2 forming $SrCO_3$ and $Sr(OH)_2$ stable compounds respectively. On the other hand, TiO_2 is chemically more stable thus having it on the surface will contribute to higher quality growth of the further layers.

To achieve TiO_2 termination, the highly reactive SrO layer is exploited by following a wet chemical etching process called buffered hydrofluoric acid (BHF). First, the $SrTiO_3$ substrate is cleaned with acetone and ethanol, then ultrasonicated in demineralized (DI) water. The ultrasonication process consists of applying ultrasonic sound waves (at frequencies higher than 20 kHz) to the solution in order to disturb the intermolecular forces reducing cluster formations [17]. This also contributes to the reaction between SrO and H_2O to produce $Sr(OH)_2$ [18].

$$H_2O \ + \ SrO \ \rightarrow \ Sr(OH)_2 \tag{3.1}$$

Next, the substrate is submerged in BHF and ultrasonicated for 30 seconds to remove the hydroxide complex exposing the TiO_2 layer [18].

$$Sr(OH)_2 \ + \ 2HF \rightarrow \ Sr^{2+} \ + \ 2F^{2-} \ + \ 2H_2O \tag{3.2}$$

3.1.2 Miscut angle

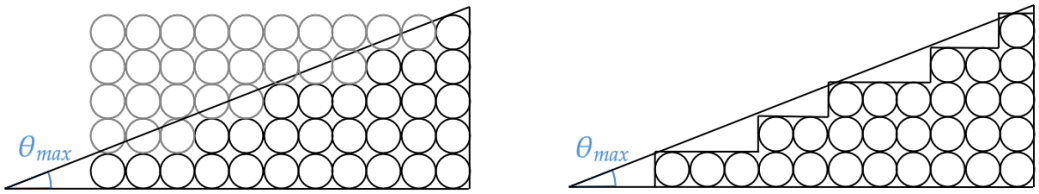

FIGURE 3.1: On the left, the structure is cut at an angle θ_{max} with respect to the crystal plane. On the right, the terraces are formed.

The surface of the substrate obtained from the manufacturer is usually not parallel to the crystalline planes. This gives rise to terrace formation, as shown in figure 3.1. The maximum angle between the crystal plane and the terrace terminations is defined as the miscut angle and is described by θ_{max} [19]. θ_{max} can be experimentally determined by scanning the surface with an atomic force microscope (AFM) and using the following equation:

$$\theta_{max} = arctan(\frac{a \cdot n}{d}) \tag{3.3}$$

where a is the step height of the terrace (which should match the lattice constant of the crystal), n is the number of terraces in the scan, and d is the width of the scan.

By scanning over different parts of the substrate, it was observed that the miscut angle was not uniform in size and density of the terraces.

3.1.3 Thermal annealing

The last step of substrate preparation is thermal annealing. It is done to remove any residue of DI water and BHF, and to improve recrystallization. The needed annealing time is dependent on the miscut angle and is determined from experimental data. The substrate used was annealed for 3 hours and 27 minutes, at 960 °C temperature, and an oxygen flow of 300 standard cubic centimeters per minute (SCCM). Annealing is performed in a rich oxygen environment to minimize oxygen vacancies.

After annealing, the substrate should have perfect terraces that are atomically flat and with a single TiO_2 termination. The step height of the terraces should be the lattice constant of $SrTiO_3$. In reality, however, mixed SrO and TiO_2 termination can take place [18], and this can be inferred from the different heights in the terrace steps.

3.2 Stack growth

Once the substrate has been prepared through the above mentioned protocols, the layers of the stack can be grown. This is done by using pulsed laser deposition (PLD) and electron beam evaporation (EBE).

3.2.1 Pulsed laser deposition

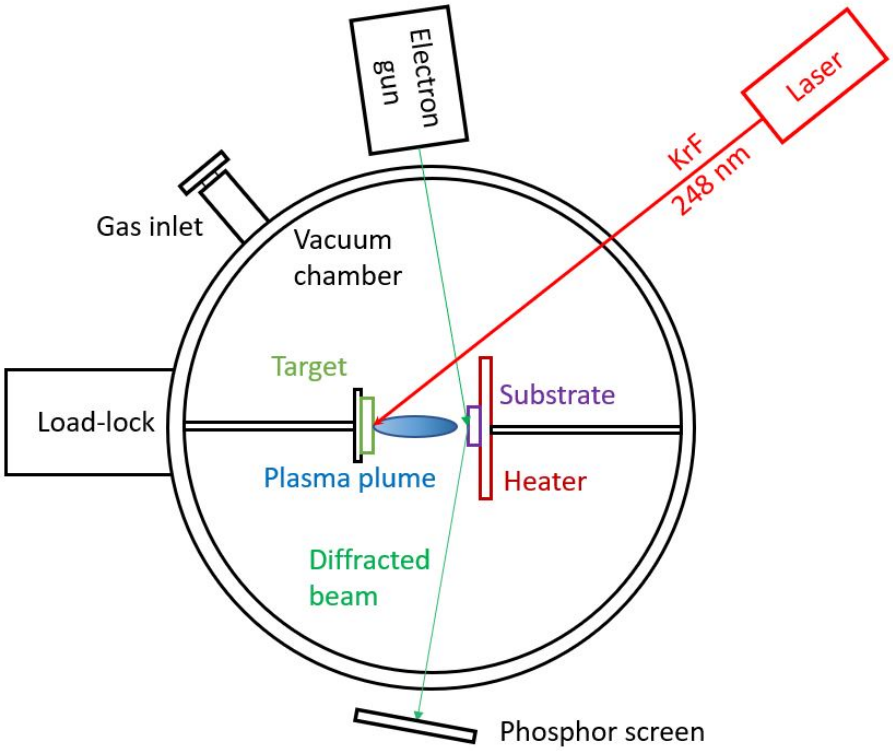

FIGURE 3.2: Experimental setup of pulsed laser deposition where all the main components are shown. The electron gun and phosphor screen from RHEED is also present in the schematic.

Pulsed laser deposition (PLD) is an advanced technique used for physical vapor deposition, which allows precise control over the thickness of deposited layers by applying small amounts of material per pulse. In PLD, a high-energy KrF laser is pulsed onto the target material, scanning across its surface. This laser energy causes the material to be removed from the target through a process called ablation, forming a plasma plume that then deposits onto the substrate.

One of the significant advantages of PLD is its ability to transfer the ablated material in a stoichiometric manner. This is primarily due to the non-equilibrium nature of the ablation process. To achieve this optimal transfer, the laser is adjusted to focus a high energy density (known as fluence) onto a small volume of the target material [20]. The size of the laser beam area is controlled using optical masks, allowing for the desired fluence. The required fluence depends on the specific target material being used.

While PLD excels in stoichiometric material transfer, when growing complex oxides, it is often necessary to perform the deposition in high oxygen (O_2) pressures. This is done to further prevent the formation of oxygen vacancies within the material, ensuring the desired composition and properties are achieved.

3.2.2 Electron beam evaporation

The deposition process starts by placing the sample in a low-pressure deposition chamber upside down. The target material is located below the sample separated by a shuttle. The evaporant is placed in a water-cooled crucible and is heated by focusing a beam of electrons on it. These electrons are thermionically emitted by a filament and are accelerated at high voltages. Then, a magnetic field redirects the beam such that it heats the center of the evaporant. The beam is set to follow an eight pattern on the evaporator to provide a more uniform heating of the material.

This process occurs in a low enough vacuum such that the air particles collide only with the walls of the container and not amongst themselves, thus increasing the mean free path of the evaporator's atoms. In depositions where a high-quality interface is needed, Ti is also evaporated. It lowers the pressure inside the chamber as it pushes possible molecules, like H_2O, to the walls of the chamber due to its heavy coating. It lowers the pressure from 10^{-6} to 10^{-7} mbar further increasing the mean free path of the evaporant's particles.

EBE uses a crystal monitor system to measure in situ how much material is being deposited. It is composed of a quartz crystal sensor, a temperature-controlled housing, and an electronic controller that makes the crystal oscillate and keeps track of it in time. Then, an internal microprocessor converts the signal into the thickness of the deposited material [21].

The deposition rate can be controlled by the software to achieve the desired quality. A slow deposition rate allows the atoms on the surface to rearrange by diffusion, facilitating the growth of a higher-quality film.

3.3 Device fabrication

The summary of the device fabrication steps is shown below and illustrated in figure 3.3:

1. Substrate preparation and stack growth.
2. UV lithography with the mask of the bottom electrode.
3. Ion beam etching down to the surface of the substrate.
4. UV lithography with the mask of the tunnel barrier ellipse.
5. Ion beam etching down to the surface of the bottom electrode.
6. UV lithography with a mask to cover the tunnel barrier ellipse and the main squares of the bottom electrode.
7. Al_2O_3 deposition by electron beam evaporation.
8. UV lithography to pattern the top electrode.
9. Electron beam evaporation of Ti and Au as a top electrode contact.

10. Wirebonding.

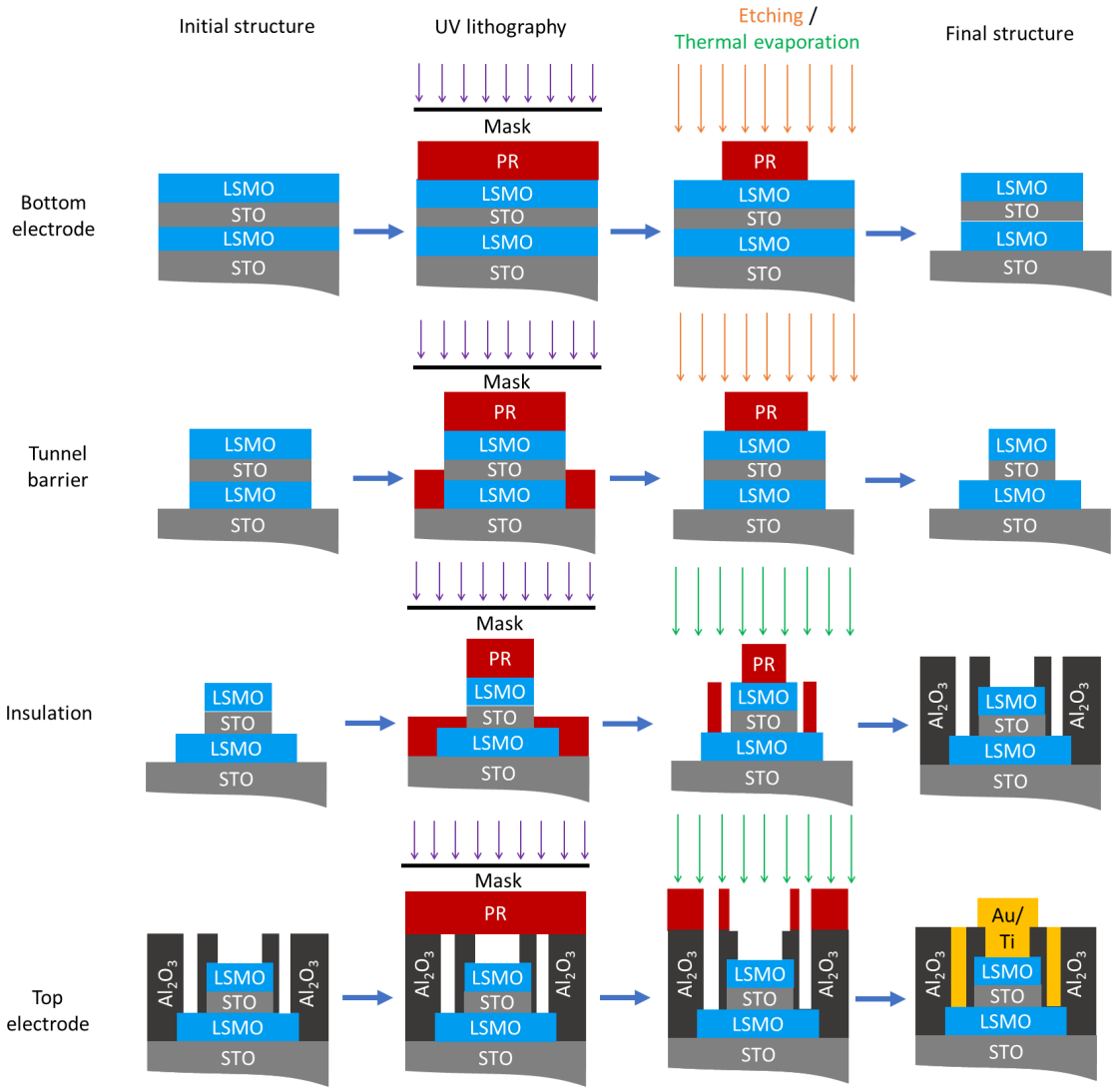

FIGURE 3.3: Schematic of the device fabrication process.

3.3.1 UV lithography

UV lithography is a parallel writing lithography technique. It produces patterns by using a photoactive compound that can dissolve or harden depending on its nature. A mask is used to choose which regions should be exposed to obtain the desired pattern.

The grown stack is first cleaned with IPA and put in a hot plate at 110°C for 1 minute to improve adhesion of the photoresist (PR) and desorb H_2O molecules that could be in the surface. The sample is then placed in a spin coater where a couple of drops of the PR AZ5214E are placed in the center. The sample is then made to spin so that the PR covers its surfaces as homogeneously as possible. The coating is followed by a soft bake to evaporate the solvent in the PR and further improve adhesion. The resultant thickness of the PR is 1.4 μm.

To print the desired patterns, a mask is aligned with the sample and exposed to UV light for 7 seconds. Since a positive photoresist has been used, the exposed areas will become more soluble. To further remove it, the sample is placed in MIF developer and DI water.

If the sample is to be etched, a hard bake step should be performed after development. This hardens the PR enough so that it will withstand the etching successfully transferring the desired pattern into the sample.

To completely remove the PR after patterning, the sample is heated in dimethylsulfoxide (DMSO) at 80ºC for 10 minutes followed by 15 minutes of ultrasonication at power 8.

3.3.2 Ion beam etching

Ion beam etching (IBE) is a method used for the removal of material from the surface of a solid. This process occurs within a low-pressure chamber where Argon gas is present. The gas is transformed into a plasma by ionization through a cathode and then accelerated by an electric field set at 25mV and 250V.

Before reaching the sample, the ions are neutralized to minimize electrostatic divergence. When a collision takes place, kinetic energy is transferred to the atoms in the lattice. If this energy surpasses the binding energy of the sample surface and the momentum is directed away from the sample, atoms will be ejected from the surface [22].

To ensure that the atoms are ejected in the desired direction, etching is performed at a 20° angle. If needed, etching at a 70° angle is carried out to eliminate any remaining traces of redeposition.

A pattern is achieved during the etching process because the photoresist (PR) material is etched at a slower rate compared to the substrate. To ensure uniform etching, the sample is rotated while the process is underway. Additionally, the ejected particles and Argon gas are actively removed from the chamber to further minimize redeposition and maintain a clean etching environment.

3.4 Structural characterization

3.4.1 Atomic Force Microscope

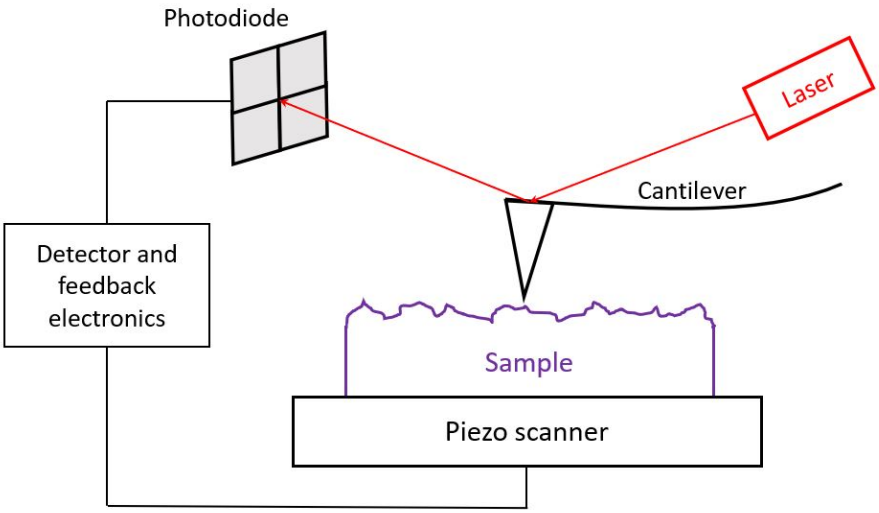

FIGURE 3.4: Schematic of the atomic force microscope setup.

The Atomic force microscope (AFM) is a scanning probe microscope that provides information about the topology of a sample. The working principle of AFM is the following. The sample to be probed is placed on a stage where two piezoelectrics will control its position with high precision. A cantilever is scanned through the sample and due to surface repulsion forces it will move mimicking the topography of the sample. This movement is detected using a laser shone into the back of the cantilever and reflected into a photodiode. The signal will then be sent to a feedback loop and the computer to process it. The operational mode chosen is tapping mode, where the cantilever is made to oscillate such that in scanning, the tip taps the surface of the sample. This mode can be in constant amplitude mode or constant frequency mode. In both cases, the feedback loop corrects possible deviations in order to maintain the desired parameter constant. The deflection is measured by the photodiode and translated into topographic information. The mode used to measure is tapping mode. Here the cantilever is made to oscillate at a constant frequency while scanning, and this is ensured by a feedback loop that corrects possible deviations.

This technique is used to measure the surface roughness of the layers grown, and the step edges from etching.

3.4.2 Reflective High Energy Electron Diffraction

Reflective High Energy Electron Diffraction (RHEED) is an in situ surface characterization technique used to monitor the growth of thin films deposited with PLD. It consists of an electron gun that projects the beam into the sample at a grazing angle, and a fluorescent screen that detects the diffracted electrons. The intensity of the spots will vary over

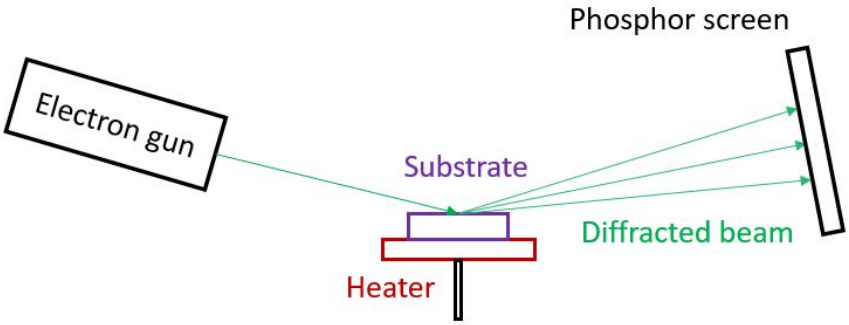

FIGURE 3.5: Experimental setup of RHEED.

time as the scattering of electrons will increase and decrease with the roughness variation of the surface. These changes describe the growth mode of the sample [23].

3.4.3 X-Ray Diffraction and X-Ray Reflectivity

X-ray diffraction (XRD) consists of a monochromatic X-ray source shone into the surface of a sample and diffracted into a detector. X-rays have enough energy to penetrate a few layers into the material so we can extract information like the out-of-plane (OOP) lattice parameter and film spacing. In order to do so, the wavelength of the source should be in the order of the lattice parameter and obey Bragg's law, described by

$$n\,\lambda\ = 2\,d\,\sin\theta \tag{3.4}$$

where n is a positive integer, λ is the wavelength of the source, d is the lattice interplanar distance, and θ is the incident angle. Bragg's law states that if the extra distance $2\,d\,\sin\theta$ the light travels to diffract from the lower lattice plane is a multiple of the wavelength, constructive interference will occur.

X-ray reflectivity (XRR) exploits the fact that when X-rays hit a surface at grazing angles, they undergo total internal reflection so XRR is related to the refractive index of the materials detected. This technique provides information like the in-plane (IP) lattice parameter, roughness at interfaces, density, and film thickness. The main difference between XRD and XRR is that, in the former, the X-ray is diffracted from the electron cloud of the lattice thus reflecting its periodicity, in the latter the variation in the index of refraction is the measured variable [24].

GenX

GenX is the software used to analyze XRR measurements. It accounts for the parameters mentioned above for all the layers of the stack. By optimizing these values, it tries to make a fit. Boundaries can be set to the values and manual optimization is also possible.

Once the fit is good enough, the optimized parameters will provide the characteristics of the stack measured.

3.4.4 Reciprocal Space Mapping

Reciprocal space mapping (RSM) is an x-ray diffraction measurement technique that scans a volume by varying both the ω and 2θ angles. This region is chosen to cover a point in reciprocal space with non-zero Miller indices for IP and OOP directions eg. the point (1,0,3). The scan gives rise to a three-dimensional image of reciprocal space from which information about the lattice parameters, strain, and film quality can be extracted from the location, and shape of the peaks obtained.

RSM relies on the fact that planes in real space can be translated into points in reciprocal space. In addition, this technique is highly sensitive to alignment, since it relies on the substrate peak being found at the location expected from its lattice constant.

3.5 Magnetic characterization

3.5.1 Magnetic Properties Measurements System

To examine the magnetic properties of LSMO thin films, a highly sensitive Superconducting QUantum Interference Device (SQUID) Magnetic Properties Measurement System (MPMS) is used. The system includes a low-pressure sample space where the samples are loaded.

Inside the system, a stepper motor induces rapid oscillation of the sample over a 5 cm distance. This motion results in a change in magnetic flux, which is then converted into a voltage signal. The system employs specialized software to analyze the signal and extract the magnetic moment information.

Throughout the measurement process, the power supply is adjusted to maintain the superconducting magnet's charge while detuning it slightly to reduce noise. This ensures that the system operates with minimal interference while retaining the necessary magnetic field strength [25].

Chapter 4

Results and Discussion

4.1 Film growth

4.1.1 Sample 1 - LSMO/STO/LSMO

The first sample was grown on a high miscut STO substrate, figure 4.4, using PLD. The sample was heated to 750 °C and deposition happened at an oxygen pressure of 0.35 mbar. A fluence of 2 J/cm^2 was used with a KrF laser of 248 nm. The frequency of the pulses was 1 Hz. For the bottom LSMO layer, 5000 pulses were applied to grow 15 nm. The tunnel barrier, STO, of 3.2 nm was grown in 403 pulses. And the top layer of 8 nm used 2500 pulses. After the growth of STO, the sample was annealed at 100 mbar of oxygen pressure for 15 min. A post-annealing process is performed. The sample is cooled down to room temperature at steps of 10 °C/min at a 100 mbar pressure of oxygen. Once the sample is cooled, it can be taken out of the chamber.

4.1.2 Sample 2 - LSMO/STO/LSMO

The second sample was also fully grown in PLD, on a low miscut STO substrate, figure 4.5. This value was used to estimate the annealing time, however, the miscut angle was inconsistent throughout the sample so it is not possible to determine a single value. The sample was heated to 750°C and grown in 0.35 mbar of oxygen. The same laser was used with a fluence of 2 J/cm^2, pulsed at 1 Hz. The bottom LSMO layer of 20 nm used 7000 pulses, the tunnel barrier of 2.7 nm used 343 pulses, and the top layer of 10 nm used 3000 pulses. After the growth of STO, the sample was annealed at 100 mbar of oxygen pressure for 15 min. A post-annealing process is carried out under the same conditions as the first sample.

4.1.3 Sample 3 - LSMO/STO/Co

The third sample used an STO low miscut substrate, figure 4.7. The first two layers were grown in PLD and the remaining ones by thermal evaporation. Once again, the sample was heated at 750°C and brought to 0.35 mbar of oxygen pressure. The same laser was used at the same frequency. For the LSMO layer, 3000 pulses were applied to grow 18 nm. To grow the 2.4 nm thick tunnel barrier, 300 pulses were used. After the growth of

STO, the sample was annealed at 100 mbar of oxygen pressure for 15 min. Subsequently, the post-annealing process is followed.

Then, by thermal evaporation, a 0.3 nm layer of Al_2O_3 was deposited, followed by 30 nm of Co, 5 nm of Ti, and 15 nm of Au.

4.2 RHEED

4.2.1 Sample 1 - LSMO/STO/LSMO

During PLD, the growth was monitored using RHEED. The intensity of the chosen diffraction spots is shown in figure 4.1. Figure 4.1A shows the variation in the intensity of the

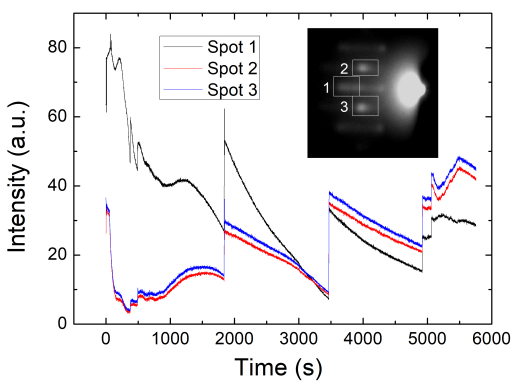

(A) Intensity signal of the bottom LSMO layer and the STO tunnel barrier for three chosen diffracted spots shown in the top right of the plot.

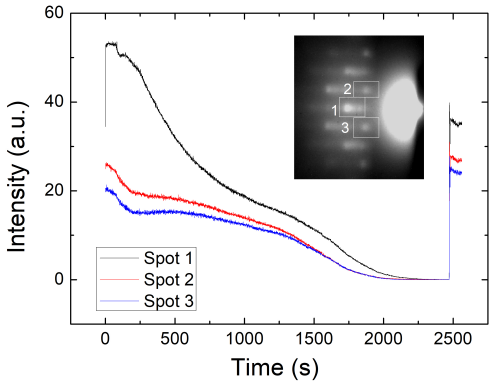

(B) Intensify signal of the top LSMO layer. The spots chosen are shown in the image at the top right of the plot.

FIGURE 4.1: RHEED measurements of all layers of the first LSMO/STO/LSMO stack.

bottom LSMO layer and of the STO tunnel barrier. No meaningful oscillations are observed thus no growth rate could be estimated. The signal starting after 5000 seconds corresponds to the growth of the STO layer, which does not allow for a growth rate estimation either. At around 2000, 3500, and 5000 seconds, there are sudden increases in intensity. This is because the setup has a defect that causes the overall intensity to decrease over time causing the loss of signal, so at those points, it has been manually increased. The issue with the setup could be due to a degradation of the electron gun filament, or of the phosphor screen. Smaller increases due to the same reason are also present at around 500 seconds.

Figure 4.1B shows the intensity variation for the top LSMO layer. There are no significant oscillations, so no growth rate can be estimated. The thicknesses mentioned in section 4.3.1 have been estimated from previously experienced growth rates of those materials. At 2500 seconds, there is a sudden increase in intensity which has been manually imparted.

4.2.2 Sample 2 - LSMO/STO/LSMO

The monitored growth is presented in figure 4.2. Figure 4.2A describes the growth of the bottom LSMO layer. The intensity shows clear oscillations up to 500 seconds, after which they are still perceived for Spot 1 but not for the other two. From these, a growth rate of 146.16 layers/second is obtained. There is a significant increase in intensity between second 1000 and 2000, after which the signal starts to stabilize. It is usual that after the first layers are deposited the oscillatory signal is lost.

Figure 4.2B presents the growth of the STO tunnel barrier. No oscillations are seen so no growth rate can be inferred. It can be seen that the pulses run until 450 seconds even though only 343 pulses were used for growth (343 seconds). This is because the signal was still being recorded for some time during the annealing process.

Figure 4.2C shows the growth of the top LSMO layer. No significant oscillations are seen, therefore no growth rate is extracted. The intensity decreases for a few hundred seconds and then significantly increases until it stabilizes around second 1500.

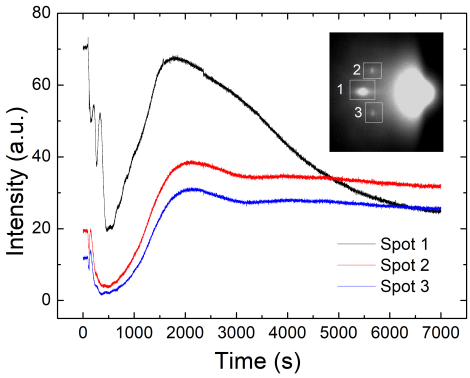

(A) Intensity signal of the bottom LSMO layer for the three chosen diffracted spots.

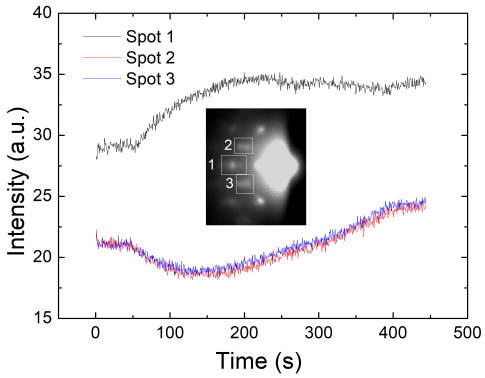

(B) Intensity signal for the STO tunnel barrier.

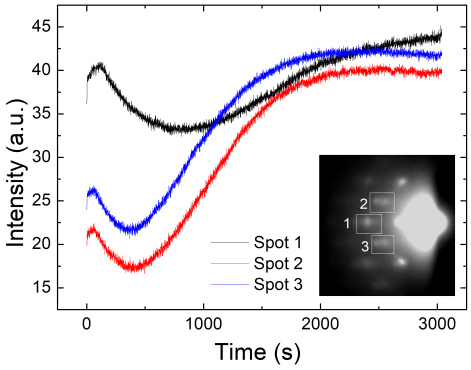

(C) Intensity signal for the top LSMO layer for the chosen diffracted spots.

FIGURE 4.2: RHEED measurements of all layers of the second LSMO/STO/LSMO stack.

4.2.3 Sample 3 - LSMO/STO/Co

The monitored stack growth is displayed in figure 4.3. Figure 4.3A shows the growth of the bottom LSMO layer, which shows very clear oscillations up to nearly 1000 seconds. A growth rate of 61.95 layers/second is extracted from these. Afterwards the signal stabilises.

Figure 4.3B shows the growth of the STO tunnel barrier. A few oscillations are present from which a growth rate of 47.88 layer/second is obtained.

The monitored intensity spots are shown in each plot.

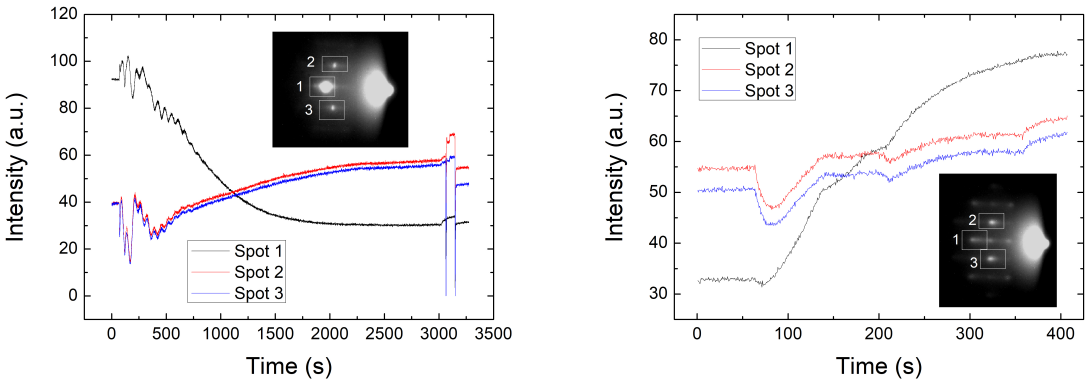

(A) Intensity signal of the bottom LSMO layer.

(B) Intensity signal of the STO tunnel barrier.

FIGURE 4.3: RHEED measurements of all layers of the LSMO/STO/Co stack.

4.2.4 Discussion

Overall, it is hard to measure clear enough oscillations to determine accurate growth rates for the second and third layers deposited. This hinders the control of growth thickness since the pulses have to be set based on past data, which does not need to give the same growth rate. For the first sample, there is a strong loss of intensity over time given by an equipment defect that is not so present in the other growths. After growing and measuring Sample 1, the PLD was deep cleaned and the electron gun filament was replaced aiming to solve the loss of intensity. These changes improved the quality of the later signals. Samples 2 and 3 show clear enough oscillations to determine a meaningful growth rate for the deposition of the bottom LSMO layer suggesting layer-by-layer growth. This is also supported by the clear three spots on the image in figures 4.2A and 4.3A. Having multiple spots can mean that there is 3D growth, which is mostly present in the tunnel barrier or bottom layer RHEED signal. 3D growth can damage the quality of the film affecting its properties. Overall, the RHEED suggests that the second LSMO/STO/LSMO sample is more epitaxial than the first and that the bottom layer of LSMO/STO/Co is of slightly higher quality than the second LSMO/STO/LSMO sample.

4.3 AFM

4.3.1 Sample 1 - LSMO/STO/LSMO

The topographic scans of the first LMSO/STO/LSMO sample are displayed in figure 4.4. Figure 4.4A shows the surface of the substrate after BHF treatment. Although not very sharp, the terraces of the substrate are well visible. Many white specks are present, which are remainders from the chemical protocol. The calculated miscut angle from this image is 0.16°. After annealing, the surface becomes cleaner and the features sharper, as shown in figure 4.4B. Finally, the fully grown stack is shown in figure 4.4C, where some grain-like features can be observed. The surface roughness was measured to be 1.789 nm.

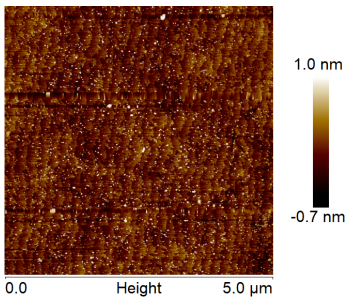

(A) 5 μm scan of the center of the sample after BHF.

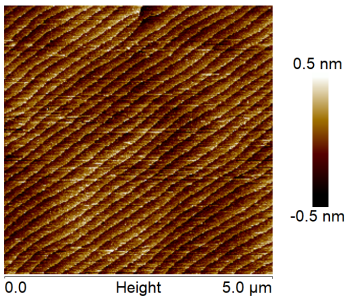

(B) 5 μm scan of the center of the sample after annealing has been performed.

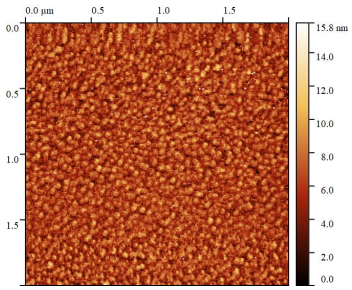

(C) 2 μm scan of the center of the first fully grown LSMO/STO/LSMO stack.

FIGURE 4.4: AFM scans of the substrate and grown stack for the first LSMO/STO/LSM sample.

4.3.2 Sample 2 - LSMO/STO/LSMO

The surface scans of the first LMSO/STO/LSMO sample are displayed in figure 4.5. The topology of the substrate after BHF treatment is shown in figure 4.5A, where some point-like features are seen, and thought to be chemical residue. The extracted miscut angle is 0.02°. Figure 4.5B shows the clean terraces of the substrate after annealing. Lastly, the fully grown LSMO/STO/LSMO stack is displayed in figure 4.5C. The measured surface roughness was 2.704 nm.

Figure 4.6 shows the heights across a line drawn in figure 4.5B. There is very inconsistent heights and only one step is close to STO's lattice parameter, 3.905 Å. This suggest double termination on the STO surface. Since after background subtraction the image was not completely clear, the step of 0.14 nm is believed to be a consequence of the tip while scanning due to its small value. A similar feature is observed close to the highest terrace in figure 4.5B.

4.3.3 Sample 3 - LSMO/STO/Co

Figure 4.7A shows the surface of the substrate after chemical etching, and the white features are remainders from it. The obtained miscut angle was 0.04°. The clean terraces

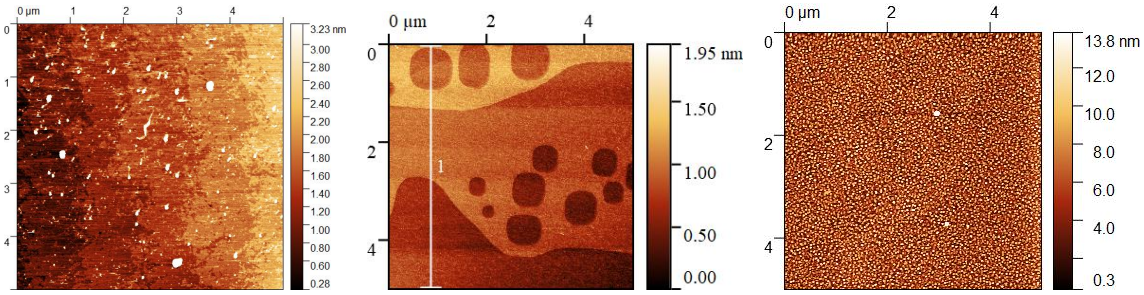

(A) 5 μm scan of the top left corner of the sample after BHF.

(B) 5 μm scan of the center of the sample after annealing has been performed.

(C) 5 μm scan of the right side of the fully grown stack.

FIGURE 4.5: AFM scans of the substrate and grown stack for the second LSMO/STO/LSMO sample.

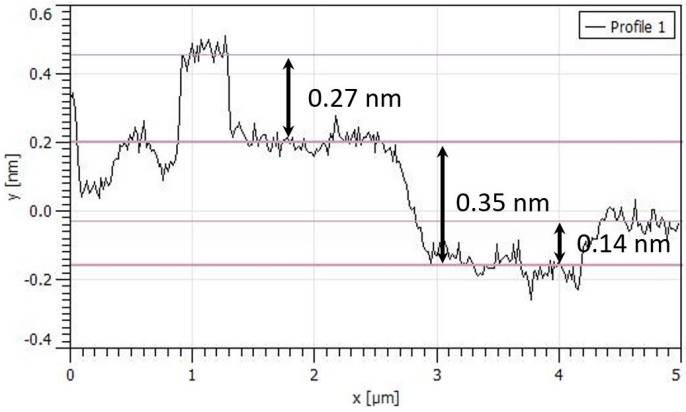

FIGURE 4.6: Heights across a profile of figure 4.5B.

after annealing can be observed in figure 4.7B. Some circular pits can be seen in the terraces. This is believed to be due to over-etching, under annealing, or a combination of both. The fully grown stack is shown in figure 4.7C, where terraces can be appreciated. These are from the substrate and seem to have clearly translated into the top layer. This is a sign of good quality growth. The measured roughness of the surface was 1.214 nm.

Figure 4.8 shows the heights across a line drawn in figure 4.5B. There is very consistent heights all around 4 nm. This is slightly above STO's lattice parameter, however the difference is only of around 0.05 nm. This suggest single termination on the STO surface.

4.3.4 Discussion

All samples show an increase in terrace sharpness after annealing, in other words, more uniform height and texture, and smoothness in the terrace edge. In addition, the substrate for sample 2 seems to be doubly terminated while the one for sample 3 is singly terminated. Between samples 2 and 3, figures 4.5B and 4.7B respectively, a difference in the shape of the terraces can be seen. Figure 4.5B have circular pits in the substrate that could come from over-etching or under-annealing while for figure 4.7B, all terraces finish in a smooth curve. In addition, grain-like features are present for the fully grown stack of the three samples. The third sample clearly displays terraces for the fully grown

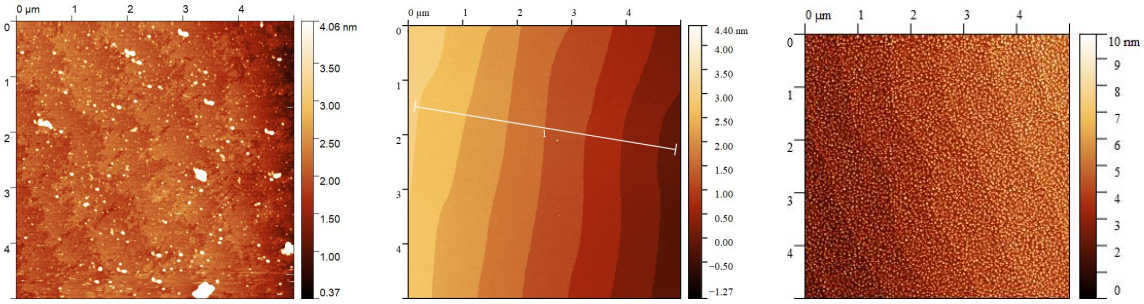

(A) AFM 5 μm scan of the top left corner of the sample after BHF.

(B) AFM 5 μm scan of the top left corner of the sample after annealing has been performed.

(C) 5 μm scan of the center fully grown stack.

FIGURE 4.7: AFM scans of the substrate and grown stack for the LSMO/STO/Co sample.

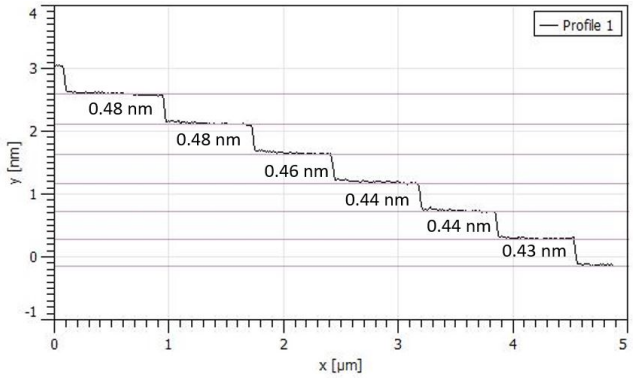

FIGURE 4.8: Heights across a profile of figure 4.7B.

stack, figure 4.7C, which is a sign of epitaxial growth. Although not so evident, a very slight terrace-like feature can be seen in the second sample, figure 4.5C, going from the bottom left to the top right of the image. Finally, no terrace features are observed in figure 4.4C for the first sample. This suggests that growth is more epitaxial, and thus of higher quality, in the last two samples. This might be due to the choice of a low-miscut substrate.

4.4 XRD and XRR

XRD shows at which degree of the scan each plane in the lattice is found for LSMO and STO layers, giving information about the interplanar distance and thus the out-of-plane lattice parameter. XRR shows the change in intensity which provides information about layer thickness, layer density, and interface roughness.

4.4.1 Sample 1 - LSMO/STO/LSMO

The peaks from the planes 001, 002, and 003 are shown for LSMO and STO in figure 4.9A. The LSMO peaks are found at 23.01°, 47.05°, and 73.58° respectively, and the STO ones at 22.76°, 46.47°, and 72.56°. The intensity of the peaks makes the signal sufficiently clear, about 10^7 and 10^4 for STO and LSMO respectively. The out-of-plane lattice parameter

obtained for LSMO was 3.680 Å and for STO 3.904 Å. The XRR signal is shown in 4.9B

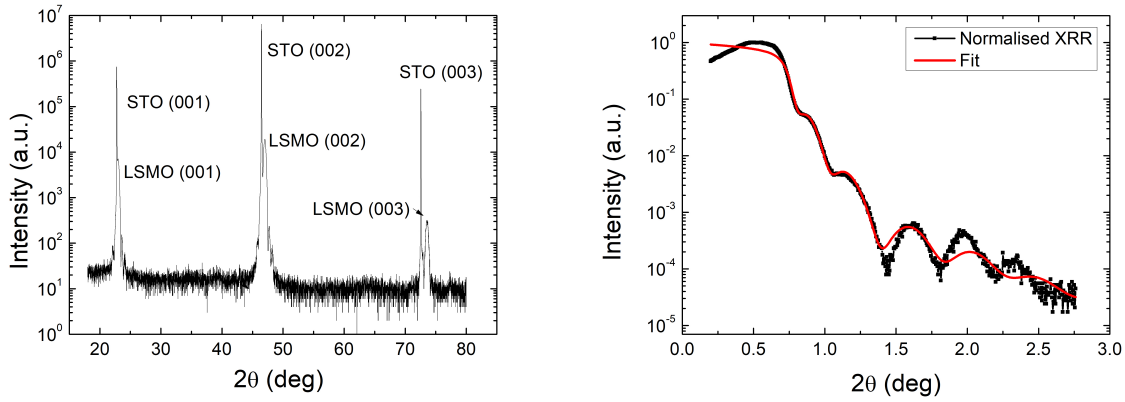

(A) XRD data showing the peaks for the 001, 002, and 003 planes of STO and LSMO.

(B) XRR data with a fit for the first LSMO/STO/LSMO stack.

FIGURE 4.9: X-ray diffraction measurements for the first LSMO/STO/LSMO sample.

together with the fit (red line). The fit has been obtained by setting some initial values of the parameters and letting GenX optimize the curve. The fit is relatively good until 1.5°. The parameters obtained from the fit of XRR are displayed in table A.2. The thicknesses of the top and bottom layer match decently well with the predicted values, however the tunnel barrier stuck to the set lower limit. The roughnesses are relatively low, the substrate being the lowest which would make sense since it was specifically treated.

4.4.2 Sample 2 - LSMO/STO/LSMO

The peak of the 002 plane is shown in figure 4.10A for STO and LSMO. They are found at 46.38°, and 47.43° respectively. The intensity of the peaks is a bit lower, about 10^5 and 10^2 for STO and LSMO respectively. The STO peak shows a double peak feature and it is not so clear to define the highest point of the LSMO peak. The out-of-plane lattice parameters extracted are 3.831 Å and 3.912 Å for LSMO and STO respectively.

The normalized XRR data is displayed in figure 4.10B. The obtained fit is reasonably good up till 2° and then it deviates from the data. The parameters obtained from the fit for XRR are displayed in table A.4. The thicknesses given match well with the predicted values, having STO on the higher side. Regarding roughnesses, one would expect that the substrate would have a lower one since it has been treated, however, it is not the case.

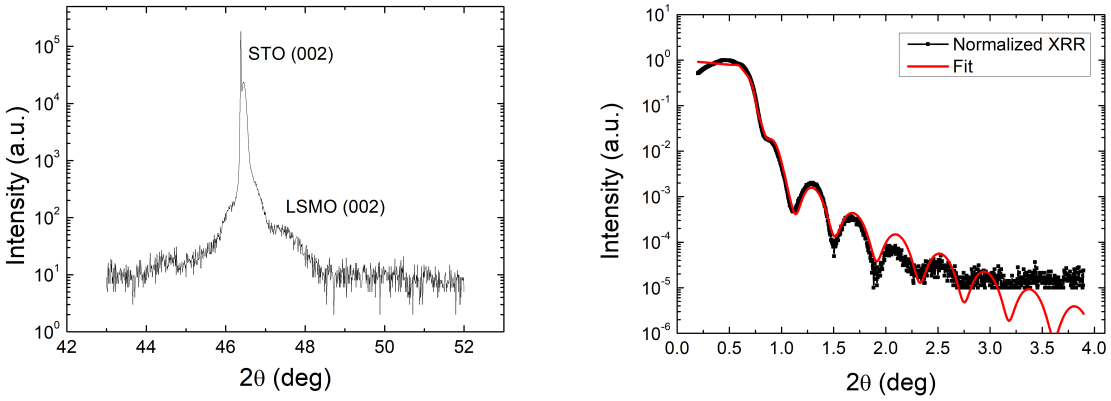

(A) XRD data showing the peaks for the 002 plane of STO and LSMO for sample 2.

(B) XRR data with a fit for the second LSMO/STO/LSMO stack for sample 2.

FIGURE 4.10: X-ray diffraction measurements for the second LSMO/STO/LSMO sample.

4.4.3 Sample 3 - LSMO/STO/Co

The peaks of the 001, 002, and 003 planes of STO and LSMO are shown in figure 4.11A. The LSMO peaks are found at 23.18°, 47.15°, and 73.76° respectively, and the STO ones at 22.78°, 45.5°, and 72.60°. They show clear peaks of about 10^6 intensity for STO and 10^2 for LSMO. The OPP lattice parameters obtained are 3.846 Å and 3.929 Å for LSMO and STO respectively.

The data and fit from XRR are plotted in figure 4.11B. The fit is okay overall with an improvement between 1.5° and 3°. The parameters obtained from the fit for XRR are displayed in table A.6. It can be noticed from the table that there is a CoO layer that was not purposefully grown. Its addition, however, improves the fit suggesting that this layer might have formed during or after growth. The thicknesses estimated approximately match the ones obtained from the fit. The LSMO, Co, and Au layers are off by about 5 nm, and the other values by less than that. The inaccuracy in the Co layer might be due to the formation of CoO at the interface. Co tends to oxidise quickly and so it has been seen in past experiments that adding this extra CoO layer to the XRR data improves the fit. In this case, the roughness of the substrate is one of the lowest among all samples.

4.4.4 Discussion

Clear XRD and XRR signals are measured. The obtained OOP lattice parameters for LSMO and STO match with their literature values of 3.88 Å and 3.905 Å respectively [26], at least up to one decimal place. The small deviations might be due to some strain in the grown films given the lattice mismatch between the different crystal structures. The fits for the XRR data are also reasonably good and the obtained parameters match decently close with those predicted by RHEED. The first sample has the best match between obtained and predicted values which may imply that growth has been of higher quality.

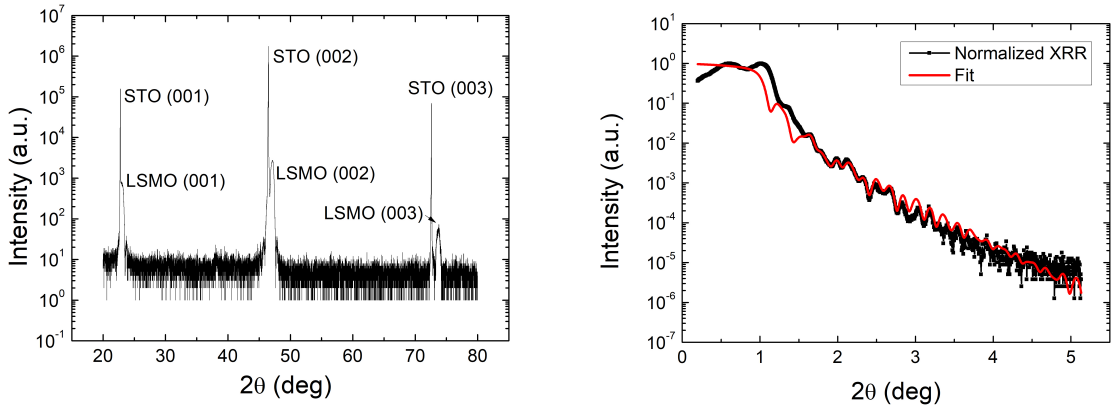

(A) XRD data showing the peaks for the 001, 002, and 003 planes of STO and LSMO.

(B) XRR data with a best fit for the LSMO/STO/Al_2O_3/Co/Ti/Au stack.

FIGURE 4.11: X-ray diffraction measurements for the LSMO/STO/Co sample.

The decrease in the peak intensity, in comparison to the first and third samples, of sample 2 could be due to a worse quality of the structure or due to a worse alignment in the setup. Overall, the quality of growth seems to be fairly good for all samples.

4.5 RSM

All scans were taken by aligning on the point with Miller indices 103.

4.5.1 Sample 1 - LSMO/STO/LSMO

Two regions of high intensity are shown in figure 4.12. The one at the bottom is the STO substrate peak and the one above corresponds to the LSMO layer. Both peaks are vertically aligned, which means that they have the same IP lattice parameter suggesting tensile strain. The STO peak has a rounder shape while the LSMO one is more elongated. The lattice parameters extracted from the image are displayed in table 4.1. The OOP ones closely match their literature value respectively, however, the IP ones are shifted towards STO's lattice parameter. There is a sharp diagonal feature crossing the center of the STO peak.

RSM 1 - LSMO/STO/LSMO					
Layer	**h**	**k**	**l**	**IP (Å)**	**OOP (Å)**
LSMO	1	0	3	3.909	3.857
STO	1	0	3	3.913	3.904

TABLE 4.1: IP and OOP lattice parameters obtained from the RSM measurements for sample 1.

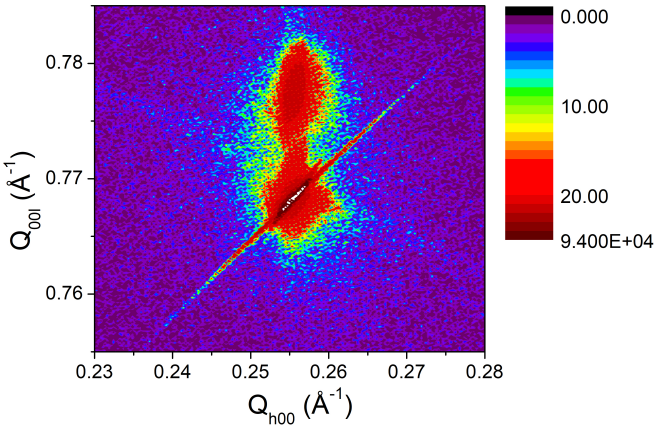

FIGURE 4.12: RSM image of sample 1 where both the STO substrate peak (bottom) and the LSMO film peak (top) are visible and vertically aligned.

4.5.2 Sample 2 - LSMO/STO/LSMO

The peak shown in figure 4.13 corresponds to the STO substrate. It can be noticed that the LSMO peak is not visible. This might be due to misalignment of the setup or due to bad quality of growth. Two sharp features are observed crossing the center of the STO peak, out of which the long one comes from an artifact of the setup. The lattice parameters extracted from the image are displayed in table 4.2. The OOP lattice parameter matches well with the literature value, however, the IP is on the higher side.

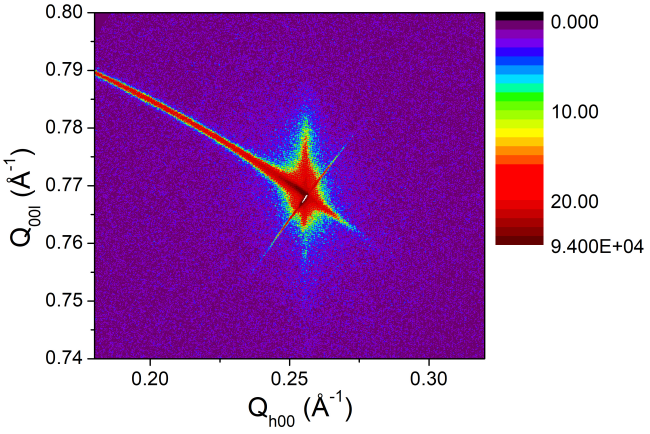

FIGURE 4.13: RSM image of sample 2 where only the STO substrate peak is visible.

4.5.3 Sample 3 - LSMO/STO/Co

The two red regions correspond to the STO substrate peak (bottom) and the LSMO peak (top) shown in figure 4.14. Both peaks are vertically aligned, which implies they have the same IP lattice parameter, thus showing epitaxial growth. The STO peak has a rounder shape while the LSMO one is more elongated. There is a sharp feature through the center

RSM 2 - LSMO/STO/LSMO					
Layer	**h**	**k**	**l**	**IP (Å)**	**OOP (Å)**
LSMO	1	0	3	-	-
STO	1	0	3	3.917	3.906

TABLE 4.2: IP and OOP lattice parameters obtained from the RSM measurements for sample 2.

of the STO peak which is believed to come from a setup artifact. The lattice parameters obtained from the image are shown in table 4.3. Both the IP and OOP match pretty well the literature values. For LSMO, the IP is higher and the OOP is lower, showing tensile strain caused by the lattice mismatch with the substrate.

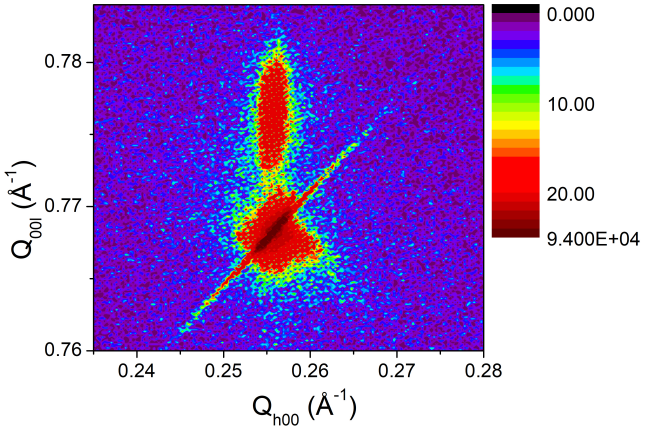

FIGURE 4.14: RSM image of sample 3 where both the STO substrate peak (bottom) and the LSMO film peak (top) are visible and vertically aligned.

RSM 3 - LSMO/STO/Co					
Layer	**h**	**k**	**l**	**IP (Å)**	**OOP (Å)**
LSMO	1	0	3	3.909	3.864
STO	1	0	3	3.909	3.905

TABLE 4.3: Lattice parameters obtained from the RSM plot in figure 4.14.

4.5.4 Discussion

Samples 1 and 3 show a bright and clear signal of both STO and LSMO peaks that are vertically aligned. This suggests epitaxial growth and thus good quality. The shape of each peak is also consistent throughout the samples. Sample 2 shows a dimmer signal in general and does not have a peak for STO, which might be due to a misalignment in the setup or due to bad quality. All samples' lattice parameters match their literature values reasonably well, with some deviations caused mainly by tensile strain. Sample 3 seems to show the best quality out of the three.

4.6 Magnetic characterization

Only measurements for sample 1 and sample 3 were taken.

4.6.1 Sample 1 - LSMO/STO/LSMO

In-plane measurements of magnetization versus temperature are shown in figure 4.15. From the hysteresis loop in figure 4.16A the saturation magnetization, remanent magnetization, and coercive field can be obtained. At 10 K these values are 566.62 emu/cm^3, 397.04 emu/cm^3, and 145 Oe for the positive side, and -571.80 emu/cm^3, -408.80 emu/cm^3, and -100 Oe for the negative side respectively. Figure 4.15B additionally shows the measurements at 200 K. The respective values obtained are 449.25 emu/cm^3, 40.53 emu/cm^3, and 8 Oe for the positive side, and -450.56 emu/cm^3, -265.17 emu/cm^3, and -1 Oe for the negative side. It is clear from the plot that all obtained values decrease with increasing temperature. In addition, it can be seen that the loops are shifted to the right with respect to the center. For the 10 K loop the shift is of 22.5 Oe, and for the 200 K loop of 3.5 Oe.

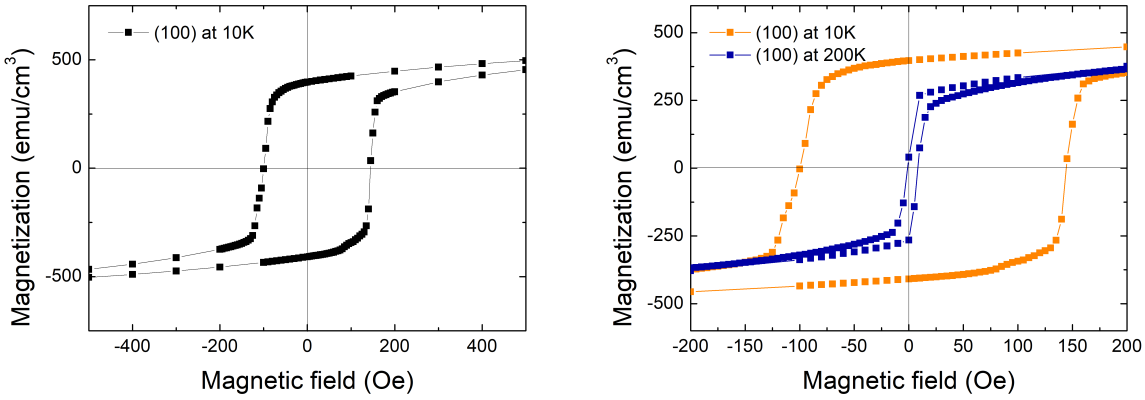

(A) M-H curve at 10 K.

(B) M-H curve at 10 K and 200 K.

FIGURE 4.15: Hysteresis loops at 10 K and 200 K for sample 1.

4.6.2 Sample 3 - LSMO/STO/Co

The in-plane measurements of magnetization versus temperature at 10 K and 200 K are shown in figure 4.16. From the hysteresis loop in figure 4.16A the saturation magnetization, remanent magnetization, and coercive field can be obtained. At 10 K these values are 983.88 emu/cm^3, 721.66 emu/cm^3, and 26 Oe for the positive side, and -983.55 emu/cm^3, -709.18 emu/cm^3, and -26.5 Oe for the negative side respectively. The values for the negative and positive regimes should be the same. The differences are small for most values, but there is a slightly higher difference for the remanent magnetization. There is a very subtle step-like feature at around 30 Oe and -30 Oe. Given that these measurements have been taken of the full stack, this feature could be the change in magnetization of the second ferromagnet as a response to the change in the magnetic field. The step is so small because the coercivities of both ferromagnets are very close together. To further check

this change, the derivative of magnetization with respect to magnetic field has been plotted in figure 4.17. The left peak corresponds to the sweep from positive to negative field and the right peak to the negative to positive. At around -35 Oe, there is a small increase in change, that could correspond to the switching of one of the ferromagnets. At -30 Oe there is a larger change that could mean the switching of the second ferromagnet. Similarly for the positive range of the magnetic field, at around 35 Oe and 30 Oe.

Figure 4.16B additionally shows the same sweep field but measured at 200 K. It is evident from the plot that there is a strong decrease in coercivity and remanent magnetization as the temperature is increased. However, there is very little change in the saturation magnetization. The saturation magnetization, remanent magnetization, and coercive filed are 922.62 emu/cm^3, 465.04 emu/cm^3 and 7 Oe for the positive side, and -923.25 emu/cm^3, -451.03 emu/cm^3 and -7 Oe for the negative side, respectively. The values for the negative and positive regimes should be the same. The differences are small for most values, but there is a slightly higher difference for the remanent magnetization.

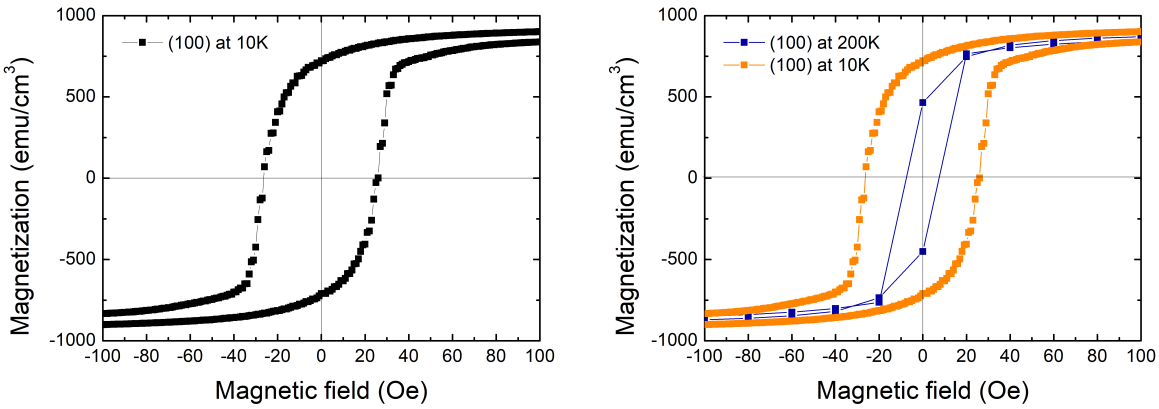

(A) M-H curve at 10 K.

(B) M-H curve at 10 K and 200 K.

FIGURE 4.16: Hysteresis loops at 10 K and 200 K for sample 3.

4.6.3 Discussion

Both samples show higher coercivity, remanence, and saturation magnetization at 10 K measurements which suggests that by increasing the temperature the magnetic response of the materials worsens. In addition, the coercivity for sample 1 is higher than sample 3, however, the saturation magnetization of sample 3 almost doubles that of sample 1. Another thing to note is that sample 1 shows a significant shift to the right with respect to the origin, that sample 3 does not have. This can be due to a magnetic coupling between both LSMO layers, in sample 1, since they are the same material. This coupling is not so strong in sample 3 since the electrodes are made of different materials. Sample 1 shows no step feature whatsoever probably because of this strong coupling. This means that the magnetization of both ferromagnets switches at the same value of magnetic field. In sample 3, the step feature shows the switching of both ferromagnets occurring at different field.

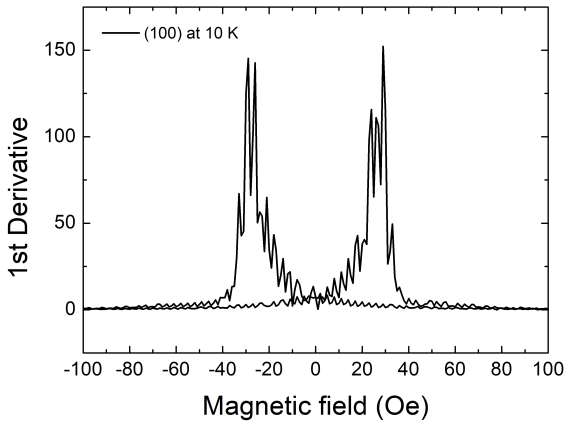

FIGURE 4.17: First derivative of the M-H curve at 10 K for the LSMO/STO/Co stack.

4.7 Electrical characterization

Current density versus voltage measurements were taken at zero field and high field only for sample 2.

4.7.1 Sample 2 - LSMO/STO/LSMO

The current density versus voltage measurements are displayed in figure 4.18. The voltage has been swept from -350 mV to 350 mV and the resulting current density has been plotted. Eight measurements have been at zero field (figure 4.18A) and at 50 Oe (figure 4.18B), at temperatures 10 K, 30 K 50 K, and 75 K. A non-linear behavior is observed in all plotted curves at higher bias, while a more linear behavior is seen close to the origin. The shape shown is expected from tunneling. It can be appreciated, from both figure 4.18A and 4.18B, that from 10 K to 50 K there are very small differences in slope. At 75 K this difference becomes larger. This is because as temperature increases, the resistance of the insulating barrier becomes smaller. Consequently, the slope of the linear regime will decrease.

The measurements with and without field have been plotted for the same temperature in figure 4.19. It can be appreciated how small the change is for 10 K, 30 K, and 50 K regardless of the presence of the field.At 75 K the difference is a bit more noticeable.

All the individual measurements have been fitted using the Simmons equation for intermediate bias, using equation 2.3. The fits are overall pretty close to the measured signal, however, it deviates at the extreme voltages. This suggests that as the high voltage regime is reached, a more adequate equation would be needed to obtain a better fit of the curves. From the fits, the values for the tunnel barrier thickness s and the potential barrier height ϕ_0 can be obtained. These values are displayed in table 4.4 for both zero field and 50 Oe measurements.

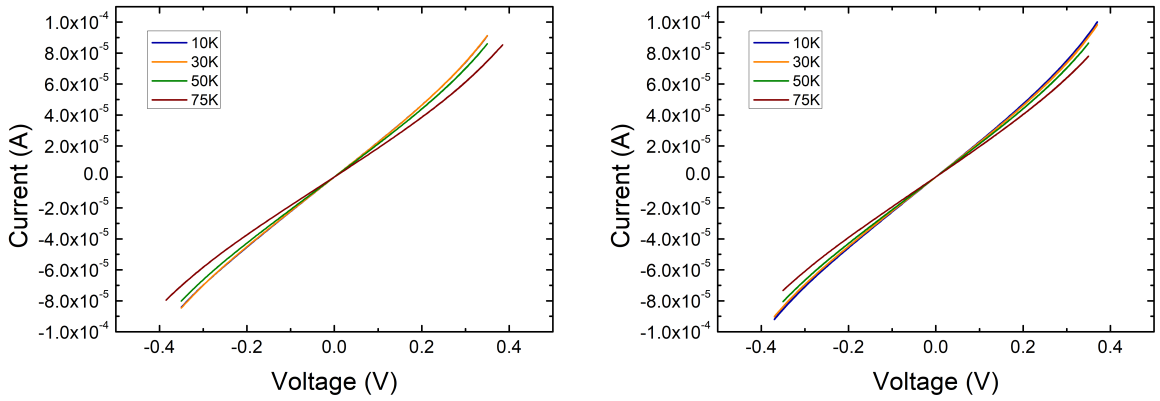

(A) Zero field measurements.

(B) Measurements at 50 Oe.

FIGURE 4.18: Current versus voltage measurements for sample 2.

	Zero field				50 Oe field			
Temperature	10 K	30 K	50 K	75 K	10 K	30 K	50 K	75 K
s (Å)	16.954	17.381	17.233	17.452	17.351	17.473	17.212	16.975
ϕ_0 (eV)	3.032	2.876	2.940	2.888	2.884	2.849	2.947	3.054

TABLE 4.4: Parameters obtained from fitting for zero field and 50 Oe measurements.

4.7.2 Discussion

Although there is a noticeable, yet relatively small, difference between the plotted curves at various temperatures. In figure 4.18A, where the magnetic field is zero and the temperatures vary, the curves for 10 K and 30 K almost completely overlap. As the temperature rises, the curve becomes more distinct. In figure 4.18B, where the magnetic field is 50 Oe and the temperatures differ, the observed differences between the curves is more prominent and follows the same trend of decreased slope with rising temperature.

Examining figure 4.19, where the field varies while maintaining the same temperature, the curves at 10 K, 30 K, and 50 K exhibit nearly complete overlap. However, at 75 K, the high field data demonstrates lower resistance in the linear regime. This suggests that increasing the magnetic field also leads to an decrease in resistance. The values obtained from the fit for the tunnel barrier thickness correspond closely to the measurements from the structural characterization.

Furthermore, the potential barrier for zero field exhibits an overall decrease in value, even though it is higher at 50 K compared to 30 K. Conversely, for 50 Oe, there appears to be an overall increase in the potential barrier, despite it decreasing at 30 K.

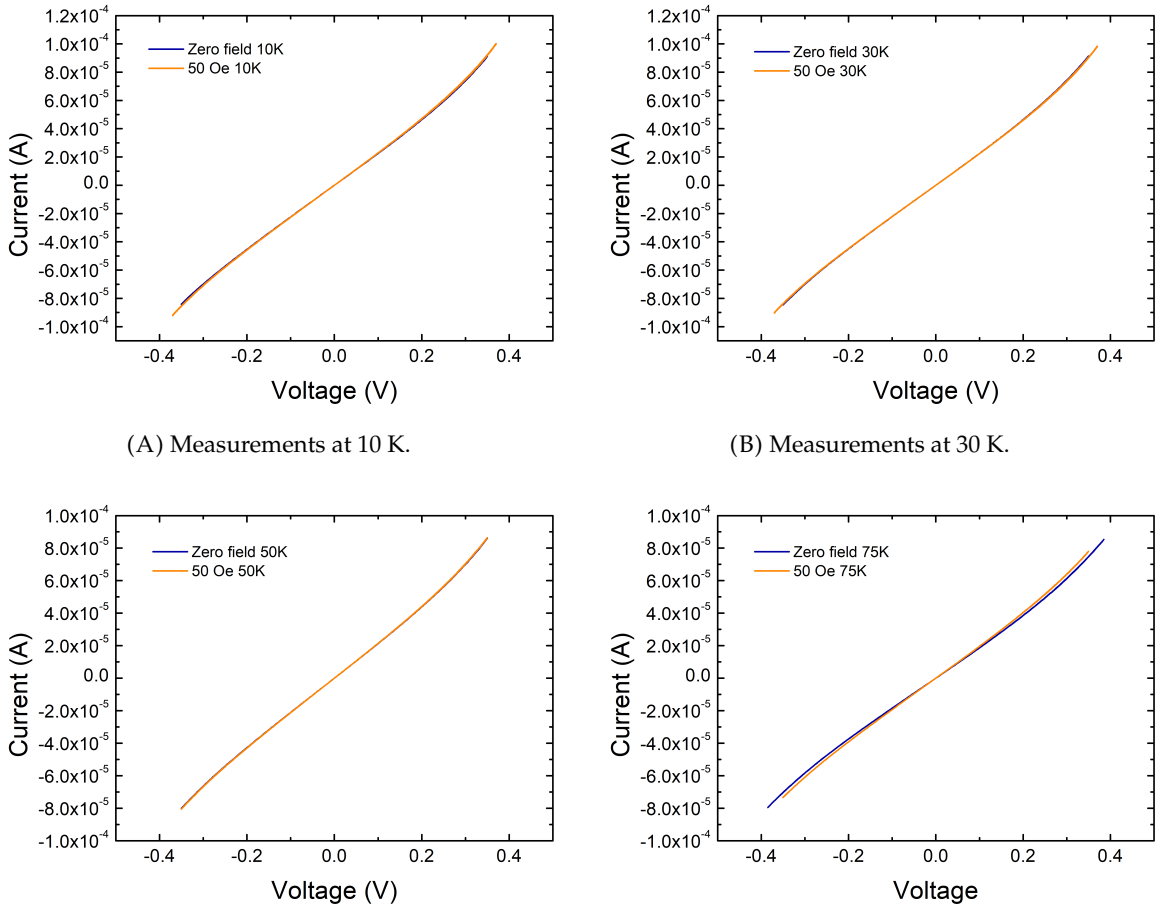

(A) Measurements at 10 K.

(B) Measurements at 30 K.

(C) Measurements at 50 K.

(D) Measurements at 75 K.

FIGURE 4.19: I-V measurements at all temperatures with and without the 50 Oe external field.

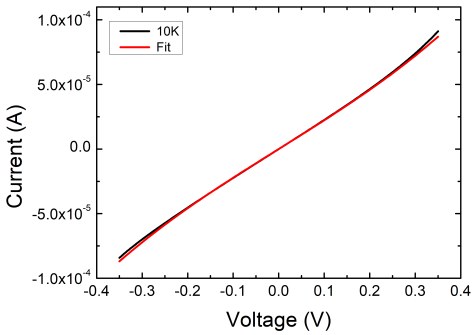

(A) Measurement taken at 10 K with zero external magnetic field.

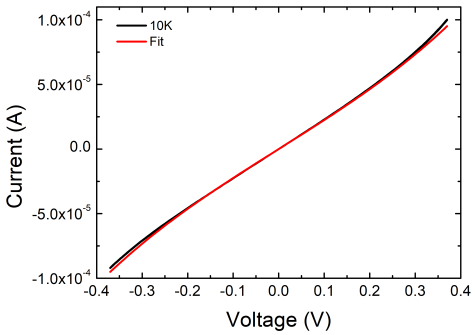

(B) Measurement taken at 10 K with an external magnetic field of 50 Oe.

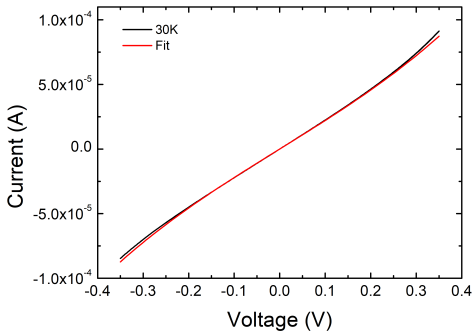

(C) Measurement taken at 30 K with zero external magnetic field.

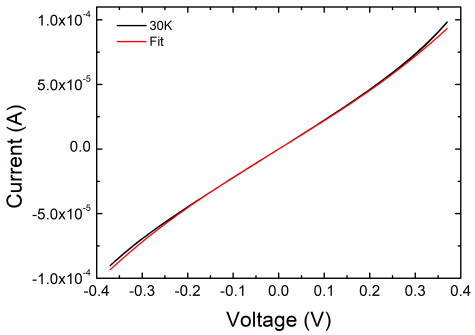

(D) Measurement taken at 30 K with an external magnetic field of 50 Oe.

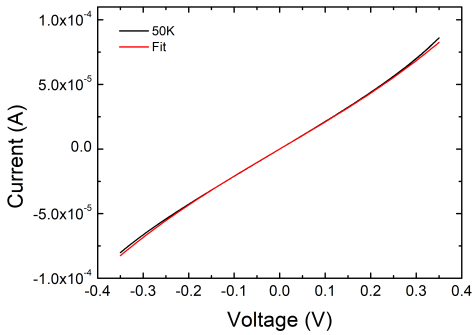

(E) Measurement taken at 50 K with zero external magnetic field.

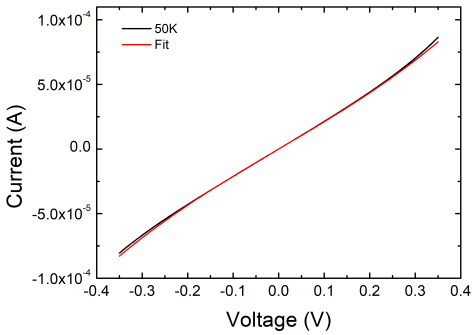

(F) Measurement taken at 50 K with an external magnetic field of 50 Oe.

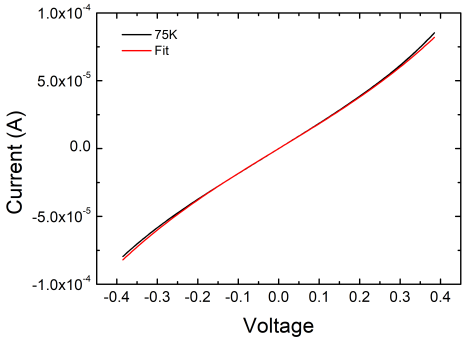

(G) Measurement taken at 75 K with zero external magnetic field.

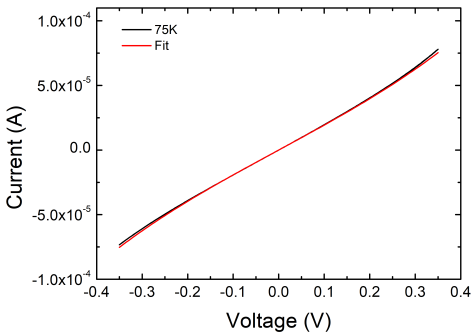

(H) Measurement taken at 75 K with an external magnetic field of 50 Oe.

FIGURE 4.20: Current versus voltage measurements at various temperatures with zero field and 50 Oe that have been fitted using Simmons model.

Chapter 5

Conclusion

Three different samples were grown on an STO substrate, two LSMO/STO/LSMO and one LSMO/STO/Co. The main difference between the two first samples is that the first used a high miscut substrate and the second one a low one. The third sample used Al_2O_3 between the STO layer and the Co bottom electrode to counter interface bonding effects. Another difference is that for magnetic measurements, the magnetic properties of the electrodes bond more significantly if the top and bottom electrode are the same material. These different combinations were chosen to study their effects in the quality of MTJ fabrication.

Growth of the LSMO and STO layers was performed using PLD and monitored with RHEED. The other layers of the third sample were deposited using EBE. Post-growth, the samples were topographically scanned using AFM and structurally characterized by XRD, XRR and RSM. It is quite complex to grow high quality films given all the factors by which quality can be affected. Firstly, during growth in PLD, it is hard to determine the exact thickness of the film if the RHEED signal does not show oscillations. In addition, while moving and manipulating the sample it might get damaged of contaminated. XRD, XRR and RSM require a very precise alignment or the desired peaks might not be visible. Lastly, device fabrication is a process that requires of precise alignment of the masks, and careful handling of the sample, as the tunnel barrier in the MTJ could be damaged, hindering the electrical measurements.

From the structural results, it can be said that all samples were successfully grown with the desired thicknesses confirmed by various measurement techniques. According to structural characterization, the LSMO/STO/Co sample shows the best epitaxial growth, followed by the first LSMO/STO/LSMO sample and the second LSMO/STO/LSMO sample. However, all three samples present good and consistent results from almost all techniques.

Based on the magnetic characterization studies, a strong magnetic coupling is measured from the first LSMO/STO/LSMO sample. From the M-H measurements, the first LSMO/STO/LSMO sample would be more suitable for spintronic applications as it has a higher coercivity providing a more stable system than a lower coercivity would, however a way

should be found to magnetically decouple the electrodes to clearly see individual switching.

From electrical characterization, it is concluded that MTJs were successfully fabricated on sample 2 out of which tunneling behavior was measured. It was also seen that the tunneling resistance increases when 50 Oe are applied, and decreases with increasing temperature.

To further complete this project, magnetic characterization should be performed to obtain the magnetization versus field plots for the second LSMO/STO/LSMO sample, and the magnetization versus temperature for all three samples. In addition, MTJs should be fabricated in samples 1 and 3 as well as be electrically measured to ultimately measure the TMR ratio in all three samples.

Appendices

Appendix A

Structural characterization

A.1 XRD and XRR

Tables with the data obtained from the plots.

A.1.1 Sample 1 - LSMO/STO/LSMO

XRD data - Sample 1	
Layers	**Average OOP (Å)**
LSMO	3.860
STO	3.904

TABLE A.1: OOP lattice parameters obtained from XRD measurements for sample 1.

XRR data - Sample 1		
Parameter	**Layers**	**Value**
Thickness (Å)	LSMO TL	70.264
	STO TB	20.000
	LSMO BL	164.905
Density (FU/Å^3)	LSMO TL	0.021
	STO TB	0.015
	LSMO BL	0.020
	STO substrate	0.017
Roughness (Å)	LSMO TL	30.905
	STO TB	57.033
	LSMO BL	72.033
	STO substrate	0.606

TABLE A.2: Parameters obtained from the XRR data fit for sample 1. TL, TB, and BL stand for the top layer, tunnel barrier, and bottom layer respectively.

A.1.2 Sample 2 - LSMO/STO/LSMO

XRD data - Sample 2	
Layers	**Average OOP (Å)**
LSMO	3.831
STO	3.912

TABLE A.3: OOP lattice parameter obtained from the XRD measurements for sample 2.

XRR data - Sample 2		
Parameter	**Layers**	**Value**
Thickness (Å)	LSMO TL	110.03
	STO TB	41.000
	LSMO BL	199.84
Density (FU/Å^3)	LSMO TL	0.0208
	STO TB	0.017
	LSMO BL	0.018
	STO substrate	0.013
Roughness (Å)	LSMO TL	37.453
	STO TB	45.554
	LSMO BL	5.0000
	STO substrate	100.00

TABLE A.4: Parameters obtained from the XRR data fit for sample 2. TL, TB, and BL stand for the top layer, tunnel barrier, and bottom layer respectively.

A.1.3 Sample 3 - LSMO/STO/Co

XRD data - Sample 3	
Layers	**Average OOP (Å)**
LSMO	3.846
STO	3.929

TABLE A.5: OOP lattice parameter obtained from the XRD measurements for sample 3.

XRR data - Sample 3		
Parameter	**Layers**	**Value**
Thickness (Å)	Au	167.05
	Ti	50.377
	Co	264.73
	CoO	32.712
	Al_2O_3	1.000
	STO	26.753
	LSMO	155.00
Density (FU/Å^3)	Au	0.048
	Ti	0.023
	Co	0.056
	CoO	0.065
	Al_2O_3	0.018
	STO	0.018
	LSMO	0.017
	STO substrate	0.021
Roughness (Å)	Au	5.315
	Ti	13.083
	Co	10.755
	CoO	7.296
	Al_2O_3	11.169
	STO	82.867
	LSMO	21.846
	STO substrate	8.4819

TABLE A.6: Parameters obtained from the XRR fit for sample 3.

Acknowledgements

I want to thank the group of Spintronics of functional materials for accompanying me in this adventure of my bachelor research project. I would like to specially thank Prof. Dr. Tamalika Banerjee for giving me the opportunity to do research in such an interesting field and surrounded by passionate people. My daily supervisor Azminul Jaman has been a great guide who I have shared laughs and helpful discussions with. Everyone in the group including Anouk Goossens, Job van Rijn, Ishitro Bhaduri, Walter and Jhe-An have contributed with valuable feedback and made my stay a more enjoyable time. It was also great to share my student experience in the group with Ayush Gupta.

Needless to say, I am immensely thankful to my parents Jacqueline Contreras and Alfredo Buil for supporting me through all my inquiries and encouraging me to chase my dreams and do better every day. Lastly, I want to thank Ishitro Bhaduri for the valuable advise, the support, and presence through the highs and lows of this journey.

Bibliography

[1] Y. Tomioka, A. Asamitsu, H. Kuwahara, and Y. Tokura, *Metal-Insulator Phenomena Relevant to Charge/Orbital Ordering in Perovskite Manganites*, pp. 155–175. Boston, MA: Springer US, 2002. pages v, 6

[2] E. Dagotto, T. Hotta, and A. Moreo, "Colossal magnetoresistant materials: the key role of phase separation," *Physics Reports*, vol. 344, no. 1, pp. 1–153, 2001. pages v, 6

[3] N. Maciel, E. Marques, L. Naviner, Y. Zhou, and H. Cai, "Magnetic tunnel junction applications," *Sensors*, vol. 20, no. 1, p. 121, 2019. pages 1

[4] S. A. Wolf, D. D. Awschalom, R. A. Buhrman, J. M. Daughton, S. von Molnár, M. L. Roukes, A. Y. Chtchelkanova, and D. M. Treger, "Spintronics: A spin-based electronics vision for the future," *Science*, vol. 294, no. 5546, pp. 1488–1495, 2001. pages 1

[5] R. Topkaya, "Tunnelling magnetoresistance at low magnetic fields in lsmo/sto/lsmo magnetic tunnel junction," *Journal of the Institute of Science and Technology*, vol. 7, pp. 125–130, 2017. pages 1

[6] E. Y. Tsymbal, O. N. Mryasov, and P. R. LeClair, "Spin-dependent tunnelling in magnetic tunnel junctions," *Journal of Physics: Condensed Matter*, vol. 15, p. R109, jan 2003. pages 1, 7

[7] M. Cesaria, A. P. Caricato, G. Maruccio, and M. Martino, "Lsmo – growing opportunities by pld and applications in spintronics," *Journal of Physics: Conference Series*, vol. 292, p. 012003, apr 2011. pages 3

[8] A.-M. Haghiri-Gosnet and J.-P. Renard, "Cmr manganites: physics, thin films and devices," *Journal of Physics D: Applied Physics*, vol. 36, p. R127, apr 2003. pages 3

[9] A. Haghiri-Gosnet, T. Arnal, R. Soulimane, M. Koubaa, and J. Renard, "Spintronics: perspectives for the half-metallic oxides," *Physica status solidi (a)*, vol. 201, no. 7, pp. 1392–1397, 2004. pages 4

[10] J. Coey and M. Venkatesan, "Half-metallic ferromagnetism: Example of cro 2," *Journal of Applied Physics*, vol. 91, no. 10, pp. 8345–8350, 2002. pages 4

[11] J. Coey and o. S. Sanvito, "Magnetic semiconductors and half-metals," *Journal of Physics D: Applied Physics*, vol. 37, no. 7, p. 988, 2004. pages 4

[12] K. M. Krishnan, *Fundamentals and applications of magnetic materials*. Oxford University Press, 2016. pages 5

[13] S. Peng, Y. Zhang, M. Wang, Y. Zhang, and W. Zhao, "Magnetic tunnel junctions for spintronics: principles and applications," *Wiley Encyclopedia of Electrical and Electronics Engineering*, pp. 1–16, 1999. pages 6, 7

[14] J. M. D. Teresa, A. Barthélémy, A. Fert, J. P. Contour, F. Montaigne, and P. Seneor, "Role of metal-oxide interface in determining the spin polarization of magnetic tunnel junctions," *Science*, vol. 286, no. 5439, pp. 507–509, 1999. pages 8

[15] A. Thomas, J. S. Moodera, and B. Satpati, "Evidence for positive spin polarization in Co with SrTiO3 barriers," *Journal of Applied Physics*, vol. 97, 05 2005. 10C908. pages 8

[16] J. G. Simmons, "Generalized formula for the electric tunnel effect between similar electrodes separated by a thin insulating film," *Journal of applied physics*, vol. 34, no. 6, pp. 1793–1803, 1963. pages 8

[17] A. K. Tiwari, A. Kumar, and Z. Said, "Synthesis, characterization, and measurement techniques for the thermophysical properties of nanofluids," in *Advances in Nanofluid Heat Transfer*, pp. 59–93, Elsevier, 2022. pages 10

[18] G. Koster, B. L. Kropman, G. J. Rijnders, D. H. Blank, and H. Rogalla, "Quasi-ideal strontium titanate crystal surfaces through formation of strontium hydroxide," *Applied Physics Letters*, vol. 73, no. 20, pp. 2920–2922, 1998. pages 10, 11

[19] J. Wang, J. Hao, J. Mu, T. Li, J. Wang, and P. Cao, "Quick determination of included angles distribution for miscut substrate," *Measurement*, vol. 89, pp. 300–304, 2016. pages 11

[20] P. Willmott and J. Huber, "Pulsed laser vaporization and deposition," *Reviews of Modern Physics*, vol. 72, no. 1, p. 315, 2000. pages 12

[21] P. Technologies, "What are quartz crystal monitoring systems aka qcm?," Oct 2017. pages 13

[22] P. G. Glöersen, "Ion - beam etching," *Journal of Vacuum Science and Technology*, vol. 12, no. 1, pp. 28–35, 1975. pages 15

[23] N. Derriche, S. Godin, R. Greenwood, A. Mercado, and A. N. Warner, "Reflection high-energy electron diffraction," 2019. pages 17

[24] M. Yasaka *et al.*, "X-ray thin-film measurement techniques," *The Rigaku Journal*, vol. 26, no. 2, pp. 1–9, 2010. pages 17

[25] A. S. Goossens, "Investigating nb-doped SrTiO3 schottky junctions as a platform for bio-inspired computing," Master's thesis, University of Groningen, Groningen, 2018. pages 18

[26] M. Španková, V. Štrbík, Š. Chromik, D. Zheng, J. Li, D. Machajdík, A. Kobzev, T. Plecenik, and M. Sojková, "Characterization of epitaxial lsmo films grown on sto substrates," *Acta Physica Polonica A*, vol. 131, no. 4, pp. 848–850, 2017. pages 27